C.E. SACLAY
DSM

SERVICE DE PHYSIQUE NUCLÉAIRE

DAPNIA-SPhN-96-10 03/1996

Reaction mechanisms in two-pion photoproduction on the proton: I - Meson exchange picture

L.Y. Murphy and J.-M. Laget

DAPNIA

Le DAPNIA (**D**épartement d'**A**strophysique, de physique des Particles, de physique **N**ucléaire et de l'**I**nstrumentation **A**ssociée) regroupe les activités du Service d'Astrophysique (SAp), du Département de Physique des Particles Elémentaires (DPhPE) et du Department de Physique Nucléaire (DPhN).

Adresse : DAPNIA, Bâtiment 141
CEA Saclay
F -9119 I Gif-sur-Yvette Cedex

Submitted to Nuclear Physics A

Reaction mechanisms in two-pion photoproduction on the proton: I- Meson exchange picture.

L. Y. Murphy *and *J.-M. Laget*

Commissariats à l'Energie Atomique,
Service de Physique Nucléaire,
Centre d'Etudes de Saclay,
91191 Gif sur Yvette CEDEX, France.

March 27, 1996

Abstract

The recent availability of more precise results for the $\gamma p \to p\pi^+\pi^-$ cross section, as well as the first ever measurements of the $\gamma p \to p\pi^0\pi^0$, and $\gamma p \to n\pi^+\pi^0$ channels calls for a revival and an extension of the effective Lagrangians model of Lüke and Söding. The updated model we present here not only accounts for the contribution of the $\Delta(1230)$ Born terms, corrected for absorptive effects, but also explicitly considers the formation of the dominant baryonic resonances in the s-channel as well as in the Born terms. The model makes use of no free parameters. While it reproduces well the $p\pi^+\pi^-$ and $p\pi^0\pi^0$ cross sections, its failure to account for half of the cross-section of the $n\pi^+\pi^0$ channel, recently determined at Mainz, is perplexing and call for further improvements. Finally, we witness, in the $\pi^0\pi^0$ channel, the fist direct evidence of the excitation of the P_{11} resonance by real photons. The extension of the model in the CEBAF energy range is also discussed.

*Present address : Department of Physics, The George Washington University, Washington DC 20052, USA

1 Introduction

Due to experimental factors. the study of double pion photoproduction reaction mechanisms on nucleons has historically been limited to the study of the $p\pi^+\pi^-$ channel. The two principal experiments relating to this subject, each performed on bubble chambers using bremsstrahlung beams [1, 2], relied on the detection of at least two charged particles to positively identify this reaction. Those involving more than one neutral particles in the final state, such as the other two possible channels, $p\pi^0\pi^0$ and $n\pi^+\pi^0$, were then deemed to be unmeasurable. Furthermore, the poor statistics characteristic of such experiments only allowed for the determination of the general trends of these processes.

It is only recently, with the advent of the high-precision tagged photon beam located at the 855 MeV CW electron accelerator MAMI-B, in Mainz, combined with the 4π detector Daphne, that more complete measurements have become possible. By not only providing better statistics, but also by the ability to detect neutral particles, a new set of constraints is available to add to our understanding of the mechanisms involved [3]. CEBAF, additional, will soon provide the opportunity to extend these studies to higher energies.

On the theoretical front, Lüke and Söding attempted to reproduce the available $p\pi^+\pi^-$ data within the framework of an effective Lagrangians model [4]. The graphs which they calculated are depicted in fig.1-I, Ha, and IIIa. It was then clearly shown that the dominant contribution was essentially due to the presence of an intermediate $\Delta^{++}\pi^-$ state. The model also accounted for unitary absorptive corrections, which are due to the coupling to other open channels. It was also shown that the formation in the s-channel (Ha) of the $D_{13}(1520)$ resonance strongly interferes with the contact term (Ia), as both lead to an S-wave $\Delta^{++}\pi^-$ final state. More recently Gomez-Tejedor and Oset [5] added many more nucleon Born diagrams, whose total contribution, however, is small. Their not accounting for unitary absorptive corrections, unfortunately, prevented them from achieving a good energy dependence, especially above 700 MeV.

We have extended the pioneering work of Lüke and Söding and considered every diagram depicted on figure 1. As such, we have explicitly included the contribution of every baryonic resonances known to decay appreciably into the double pion channel [6] and which is strongly coupled to the γN channel [7]. This is meant to include decays into the usual $\Delta\pi$ channel, as well as decays into nucleon-meson systems. Since we are primarily interested here in the Mainz energy range, we consider only the $P_{11}(1440)$, $D_{13}(1520)$ and $D_{33}(1700)$ resonances. Some, such as the $S_{11}(1535)$, decay almost exclusively in the πN and ηN channels and others, as the $P_{33}(1600)$ or S_{31} (1620), have vanishing radiative decay widths and need not be added into our analysis. We have not considered the contribution of the $F_{15}(1700)$, which mainly decays in the $N\rho$ channel ; it will be considered elsewhere. Two new features of our

Resonance	Mass in MeV/c^2	Central Mass Widths in MeV					
		Full	Partial				
		r	$\Gamma_{\pi\Delta}$	$\Gamma_{\gamma\pi}$	$\Gamma_{\rho N}$	$\Gamma_{\sigma N}$	$\Gamma_{\pi N}$
D_{13}	1520.	120.	24.	.3	24.	0.	72.
D_{33}	1700.	300.	150.	.9	24.	0.	81.
P_{11}	1440.	350.	88.	.3	0.	43.	220.

Table 1: Parameters of the resonances used in the model.

model are the Born terms (fig.1-IV) associated to each baryonic resonance and the ρ contact term which contributes only in the $n\pi^0\pi^+$ channel.

It is the philosophy of this article to fix the numerical values of each of the parameters associated with the resonances, listed in table 1, to those found in the literature [6, 7, 8]. We stress, therefore, that we rely on no free parameters to fit the model to the available data.

2 The Model

2.1 Notations and cross-sections

We adhere to the convention defined by Bjorken and Drell and use their normalizaion factors, as well as set $\hbar$ = c = 1. We introduce now the notation which will be found throughout this article. Every kinematical quantity is calculated in the laboratory frame unless otherwise specified. Stared quantities are evaluated in the rest frame of the πN resonant state, be it a Δ, a D_{13}, a D_{33}, or a P_{11}. $\vec{k}$, and $\vec{\epsilon}$ *are* respectively the momentum and the polarization of the photon. $(\mu^o_{1,2}, \vec{\mu}_{1,2})$ are the 4-vector momenta of the two pions according to the convention shown in the diagrams of figure 1. $E_{i,f}$, and $m_{i,f}$ are the energy and masses of the target and outgoing nucleon, and $\vec{p}_f$ stands for the momentum of the outgoing nucleon. m_π is the mass of the pion. $\vec{S}$ is the spin 3/2 to spin 1/2 transition operator. Q is the total pion-nucleon (A) energy in the barycentric system, defied as $Q^2 = (p^o_\Delta)^2 - |\vec{p_\Delta}|^2$. χ_i and χ_f are the magnetic quantum numbers of the nucleon in the initial and the final state. M_X, and Γ_X stand for the mass and the full width of the X-resonance. W is the total available energy of the system. Finally, h& is the invariant mass of the $\pi\pi$ system, while m_σ, and m_ρ are the on-shell masses of the σ and p mesons. The parameters describing these mesons are listed in table 2

The complete expression describing the cross-section is:

$$d\sigma = (2\pi)^4\delta^4(P_i - P_f)\left(\frac{1}{2k}\right)\left(\frac{m_i}{E_i}\right)\left(\frac{1}{2\mu^o_1}\right)\left(\frac{1}{2\mu^o_2}\right)\left(\frac{m_f}{E_f}\right)$$

Meson	Mass in MeV/c^2	Full width in MeV
ρ	770.	151.
σ	800.	800.

Table 2: Parameters of the mesons used in the model

Graph		$p\pi^+\pi^-$		$n\pi^0\pi^+$		$p\pi^0\pi^0$
		$p\pi^+)\ \pi^-$	$(p\pi^-)\ \pi^+$	$n\pi^0)\ \pi^+$	$n\pi^+)\ \pi^0$	$p\pi^0)\ \pi^0$
Born Δ	C_π	-1	$\frac{1}{3}$	$\frac{\sqrt{2}}{3}$	0.	0.
$D_{13} \to \pi\Delta$	C_D	$-\frac{1}{\sqrt{2}}$	$-\frac{1}{3\sqrt{2}}$	$-\frac{1}{3}$	$\frac{1}{3}$	$-\frac{\sqrt{2}}{3}$
$P_{11} \to \pi\Delta$	C_D	$-\frac{1}{\sqrt{2}}$	$-\frac{1}{3\sqrt{2}}$	$-\frac{1}{3}$	$\frac{1}{3}$	$-\frac{\sqrt{2}}{3}$
$D_{13} \to \rho N$	C_ρ	$-\frac{1}{\sqrt{6}}$	0.	$\frac{1}{\sqrt{3}}$	0.	0.
$P_{11} \to \sigma N$	C_σ	$\frac{1}{\sqrt{3}}$	0.	0.	0.	$-\frac{1}{\sqrt{3}}$
$D_{33} \to \pi\Delta$	C_D	$-\sqrt{\frac{2}{5}}$	$\sqrt{\frac{8}{45}}$	$\frac{4}{3\sqrt{5}}$	$-\frac{1}{3\sqrt{5}}$	$\sqrt{\frac{2}{45}}$
Born P_{11}	C_B	0.	2	$-\sqrt{2}$	0.	0.
Born D_{13}	C_B	0.	2	$-\sqrt{2}$	0.	0.
ρ contact	C'_ρ	0.	0.	1.	0.	0.
ρ diffractive	C''_ρ	1.	0.	0.	0.	0.

Table 3: Isospin coefficients

$$\times \frac{1}{(2\pi)^9} d\vec{\mu_1} d\vec{\mu_2} d\vec{p} \frac{1}{2}\frac{1}{2} \sum_{\text{spins}} |\mathcal{T}_{FI}(\vec{\mu_1}, \vec{\mu_2}) + \mathcal{T}_{FI}(\vec{\mu_2}, \vec{\mu_1})|^2 \tag{1}$$

where the two $\frac{1}{2}$ factors are the averages taken over the spin of the nucleon and the photon polarization. Integrating over the momenta of each undetected particle lead to the various differential and integrated cross-sections. $\mathcal{T}_{FI}$ is the coherent sum of the matrix elements describing the various reaction channels, which we will now write out explicitly.

2.2 The $\pi\Delta$ Born terms

The diagrams corresponding to the $\pi\Delta$ Born terms are depicted on fig.1-I. The contact diagram leads solely to a S-wave $\Delta\pi$ final state. A rapid rise in cross-section as a function of energy is generally considered to be a direct manifestation of this term. The pion exchange term, on the other hand, leads to S, P and higher orbital angular momenta in the final state, and rises more smoothly. The last two terms, though strictly required to insure gauge invariance, are numerically unimportant in our energy range [4]. In the following discussion we will only concentrate on the contact and the pion exchange terms and ignore any possible contribution from the

other two diagrams.

The matrix element, subject to the above conditions, then takes the form [9]:

$$\mathcal{T}(\vec{\mu_1},\vec{\mu_2}) = -eC_\pi G_3^2 \frac{2Q}{Q^2 - M_\Delta^2 - iM_\Delta\Gamma_\Delta}\sqrt{\frac{E_i+m_i}{2m_i}}\sqrt{\frac{E_f+m_f}{2m_f}} \times \left\langle \chi_f \left| \vec{S}\cdot\vec{\mu_2}\vec{S}^\dagger \cdot \left[\frac{(\vec{\mu_1}^* - \vec{k}^*)(2\vec{\mu_1}-\vec{k})\cdot\vec{\epsilon}}{(\mu_1-k)^2 - m_\pi^2} + \vec{\epsilon}\right]\right| \chi_i \right\rangle \tag{2}$$

where C_π reflects the isospin structure of the vertex. Its values, depending on the reaction, are listed in table 3. G_3 is the $\pi N\Delta$ coupling constant and Γ_Δ is the energy dependent A width, as defined in ref [10]. Note that the first term in the bracket corresponds to the pion exchange Born term while the second corresponds to the contact Born term.

2.3 The $D_{13} + \pi\Delta$ channel

The D_{13} resonance is excited both by Electric and Magnetic multiples. Their radiative widths are respectively $\Gamma_\gamma^E = 0.315$ MeV and $\Gamma_\gamma^M \simeq 0.210$ MeV [7]. They are related to the corresponding coupling constants by:

$$\Gamma_\gamma^E = \frac{1}{3\pi} e^2 G_\gamma^{E^2} \frac{m_i}{M_{D_{13}}} k$$

and

$$\Gamma_\gamma^M = \frac{3}{4\pi} e^2 G_\gamma^{M^2} \frac{m_i}{M_{D_{13}}} \frac{k^3}{(m_i + \text{'\&3})^2}$$

Ultimately, the D_{13} decays appreciably into $\pi\Delta$ S and D states. The corresponding partial widths are respectively [6] $\Gamma_{\pi\Delta}^S \simeq 7 \pm 4$ MeV and $\Gamma_{\pi\Delta}^D \simeq 18 \pm 5$ MeV, and are related to the corresponding coupling constants by:

$$\Gamma_{\pi\Delta}^S = \frac{1}{2\pi}\frac{M_\Delta}{M_{D_{13}}} G_\pi^{S^2} \mu_1$$

and

$$\Gamma_{\pi\Delta}^D = \frac{2}{3\pi}\frac{m_\pi^2 + \mu_1^2}{M_{D_{13}} M_\Delta} G_\pi^{D^2} \mu_1^5$$

The matrix elements, depicted in fig.1.IIa, describing the electric excitation of the D_{13} resonance related to its decay have the same structure and may be combined in the same compact form:

$$\mathcal{T} = C_D e G_\gamma^E G_3 G_3^* \frac{2Q}{(Q^2 - M_\Delta^2 + iM_\Delta\Gamma_\Delta)} \frac{2W}{(W^2 - M_{D_{13}}^2 + iM_{D_{13}}\Gamma_{D13})} \times$$

$$\sqrt{\frac{E_i+m_i}{2m_i}}\sqrt{\frac{E_f+m_f}{2m_f}}\left\langle \chi_f \left| \vec{S}\cdot\vec{\mu}_2^{*}\vec{S}^{\dagger}\cdot\vec{\epsilon}\right| \chi_i \right\rangle \tag{3}$$

provided that

$$G_3^{*} = G_\pi^S + \frac{2}{3}G_\pi^D\mu_1^2\frac{\sqrt{m_\pi^2+\mu_1^2}}{M_\Delta}$$

The isospin coefficient C_D is listed in table 3.

It is worth pointing out that Eq. 3 clearly exhibits the same structure as the contact part of Eq. 2. This is the origin of the well known maximum interference between the D_{13} s-channel formation term and the Born contact term.

The matrix element corresponding to the magnetic excitation of the D_{13} resonance is obtained in the same way, but is not explicitly written here.

2.4 The $D_{13} \rightarrow N\rho$ channel

The D_{13} resonance has also been found [6] to decay in the $N\rho$ channel. The matrix element describing this channel, as depicted on fig.1.IIb, is given by:

$$\begin{aligned}\mathcal{T} &= C_\rho g_{\rho\pi\pi}\left(eG_\gamma^E\right)g_\rho^{*}\sqrt{\frac{E_i+m_i}{2m_i}}\sqrt{\frac{E_f+m_f}{2m_f}}\times \\ &\frac{1}{M_{\pi\pi}^2-m_\rho^2+im_\rho\Gamma_\rho}\frac{2W}{W^2-M_{D_{13}}^2+iM_{D_{13}}\Gamma_{D13}}\left\langle \chi_f\left|\vec{S}\cdot(\vec{\mu}_1-\vec{\mu}_2)\vec{S}^{\dagger}\cdot\vec{\epsilon}\right|\chi_i\right\rangle\end{aligned} \tag{4}$$

the isospin coefficient C_ρ is listed in table 3, and G_γ^E is the coupling constant at the γpD_{13} vertex. The coupling constant $g_{\rho\pi\pi}$ describing the decay of the ρ into two pions is related to its width Γ_ρ via

$$\Gamma_\rho = \frac{1}{12\pi}\frac{g_{\rho\pi\pi}^2}{m_\rho^2}k^3$$

The coupling constant g_ρ^{*} describing the decay of the D_{13} into the p-nucleon system is related to the corresponding width by

$$\Gamma_{\rho N} = \frac{(g_\rho^{*})^2}{12\pi}\frac{(E_f+m)}{M_{D13}}\rho(W)$$

p(W) is the momentum of the p-meson weighted by its mass distribution, as per ref [6]. It takes the form:

$$\rho(W) = \int_{2m_\pi}^{W-m}\frac{q}{2\pi}\frac{\Gamma_\rho}{(Q-m_\rho)^2+(\Gamma_\rho/2)^2}dQ$$

where Q stands here for the mass of the $\pi\pi$ system, and q is its total moment urn in the D_{13} rest frame.

2.5 The D_{33} decay channels

The expression for the amplitudes of these channels is given by Eqs. 3 and 4, with the relevant values of the mass and coupling constants listed in tables 1 and 3.

2.6 The $P_{11} \rightarrow \pi\Delta$ channel

The matrix element describing this channel, shown on fig.1-IIIa, with the intermediate P-wave $\pi\Delta$ state, is written:

$$\mathcal{T} = \frac{ieG_\gamma^P G_\pi C_D 2W 2Q}{(W^2 - M_{P11}^2 - iM_{P11}\Gamma_{P11})(Q^2 - M_\Delta^2 - iM_\Delta\Gamma_\Delta)} \times \sqrt{\frac{E_i + m_i}{2m_i}}\sqrt{\frac{E_f + m_f}{2m_f}} \left\langle \chi_f \left| \vec{S} \cdot \vec{\mu_2^*} \vec{S}^\dagger \cdot \vec{\mu_1^*} \vec{\sigma} \cdot \vec{k} \times \vec{\epsilon} \right| \chi_i \right\rangle \tag{5}$$

where C_D is the isospin constant as per eq. 3. We identify G_π as being related to the partial width &, listed in table 1, by:

$$\Gamma_{\Delta\pi} = \frac{1}{\pi} G_\pi^2 \frac{M_\Delta}{M_{P11}} (\mu_1)^3$$

and G_γ^P by:

$$\Gamma_{\gamma p} = \frac{e^2}{3\pi} (G_\gamma^P)^2 (k)^3 \frac{m}{M_{P11}}$$

In order to reflect the relative phase of the experimental multiples [6], and partial waves (7], G_γ^P should be < 0. The total width Γ_{P11} is taken with the appropriate energy dependence.

2.7 The $P_{11} \rightarrow N\sigma$ channel

The P_{11} resonance has also been found to decay into a $N(\pi\pi)^{I=0}_{S-wave}$ mode [6]. We have accordingly parameterized this $(\pi\pi)^{I=0}_{S-wave}$ state by the so-called σ particle, as shown on fig. 1-IIIb. The matrix element for this channel is written as:

$$\mathcal{T} = ieg_{\sigma\pi\pi} m_\sigma G_\gamma^P C_\sigma g_\sigma^* \sqrt{\frac{E_i + m_i}{2m_i}}\sqrt{\frac{E_f + m_f}{2m_f}} \times \frac{1}{M_{\pi\pi}^2 - m_\sigma^2 + im_\sigma\Gamma_\sigma} \frac{2W}{W^2 - M_{P11}^2 + iM_{P11}\Gamma_{P11}} \left\langle \chi_f \left| \vec{\sigma} \cdot \vec{k} \times \vec{\epsilon} \right| \chi_i \right\rangle \tag{6}$$

where G_γ^P describes the $\gamma p P_{11}$ vertex. C_σ is the usual isospin coefficient. The coupling constant $g_{\sigma\pi\pi}$ is related to the decay width of the σ into two pions

$$\Gamma_\sigma = \frac{g_{\sigma\pi\pi}^2}{4\sqrt{2}\pi} k$$

and g_σ^* is related to the decay width of the P_{11} into a σ-nucleon system

$$\Gamma_{N\sigma} = \frac{(g_\sigma^*)^2}{6\pi} \frac{m}{M_{P11}} \rho(W)$$

2.8 The ρ contact term

It is necessary to include ρ production Born mechanisms. To date, we have only included the contact term (fig.1-V). It contributes only in channels where a charged ρ can be produced. The matrix element is:

$$\mathcal{T} = eC_\rho' \frac{g_\rho(1+\kappa_\nu)}{2m} g_{\rho\pi\pi} \frac{\langle \chi_f | \vec{\sigma} \cdot \vec{\epsilon}_\gamma \times (\vec{\mu}_1 - \vec{\mu}_2) | \chi_i \rangle}{M_{\pi\pi}^2 - m_\rho^2 + i m_\rho \Gamma_\rho} \sqrt{\frac{E_i + m_i}{2m_i}} \sqrt{\frac{E_f + m_f}{2m_f}}$$

where C_ρ' is the isospin coefficient, and, as found in ref [11], $g_\rho^2/4\pi = 0.40$, and $\kappa_\nu = 6$.

2.9 The diffractive ρ production term

In our analysis, we have assumed that the ρ meson is diffractively produced via the exchange of the Pomeron, and subsequently decays into a $\pi^+\pi^-$ pair. The corresponding amplitude is:

$$\mathcal{T} = C_\rho'' g_{\rho\pi\pi} \left(\frac{q_\rho}{k}\right)_{c.m.} \frac{1}{M_{\pi\pi}^2 - m_\rho^2 + i m_\rho \Gamma_\rho} \vec{J}_{\gamma p \to p\rho} \cdot (\vec{\mu}_1 - \vec{\mu}_2) \tag{7}$$

where $\vec{J}_{\gamma p \to p\rho} \cdot \vec{\epsilon}_\rho$ is given by Eq. B.8 in Ref. [12]. Since this amplitude leads to a constant cross-section with varying photon energy, we've 'resorted to multiplying it by the $\left(\frac{q_\rho}{k}\right)_{c.m.}$ factor so as to reproduce its proper threshold behavior.

2.10 The πD_{13} Born term

As the model is extended to higher energies, we find it necessary to introduce terms of the $\pi\Delta$ Born type, substituting the various resonances for the A (fig.1-IV). Once again, we only calculate the contact, and pion exchange terms. We get:

$$\mathcal{T} = -\frac{2WeG_{D_{13}}^2 C_B}{W^2 - M_{D_{13}}^2 + iM_{D_{13}}\Gamma_{D13}} \sqrt{\frac{E_i + m_i}{2m_i}} \sqrt{\frac{E_f + m_f}{2m_f}} \times$$

$$\langle \chi_f | \vec{\sigma} \cdot \left[\frac{\vec{R}}{E_{D_{13}} + M_{D_{13}}} - \frac{\vec{p_f}}{E_f + m_f} \right] \vec{S} \cdot \vec{\mu_2}$$
$$\vec{S}^\dagger \cdot \left[\vec{\epsilon} + \frac{\vec{R}(\vec{\epsilon} \cdot \vec{R})}{M_{D_{13}}(E_{D_{13}} + M_{D_{13}})} - \vec{q}^* \frac{(2\vec{\mu}_1 - \vec{k}) \cdot \vec{\epsilon}}{(q^*)^2 - m_\pi^2} \right] \vec{\sigma} \cdot \left[\frac{\vec{p_i}}{E_i + m_i} - \frac{\vec{R}}{E_{D_{13}} + M_{D_{13}}} \right] |\chi_i\rangle \tag{8}$$

where stared quantities are now calculated in the D_{13} resonance rest frame. $\vec{R}$ stands for the momentum of the emitted resonance. C_B is the isospin coupling constant. The coupling constant $G_{D_{13}}$ is related to πN partial decay width through

$$\Gamma_{\pi N} = \frac{G_{D_{13}}^2}{12\pi} \frac{q^{*5}}{M_{D_{13}}(E_f + m_f)}$$

One recognizes, in the second to last bracket of Eq. 8, the contact term (proportional to $\vec{S}^\dagger \cdot \vec{\epsilon}$) and the pion exchange term.

2.11 The πP_{11} Born term

In a similar fashion we compute the matrix element for the πP_{11} Born term. The element takes the form:

$$\begin{aligned} \mathcal{T} = & \frac{-2Weg^{*2}C_B}{W^2 - M_{P_{11}}^2 + iM_{P_{11}}\Gamma_{P_{11}}} \sqrt{\frac{E_i + m_i}{2m_i}} \sqrt{\frac{E_f + m_f}{2m_f}} \times \\ & \langle \chi_f | \vec{\sigma} \cdot \left[\frac{\vec{R}}{E_{P_{11}} + M_{P_{11}}} - \frac{\vec{p_f}}{E_f + m_f} \right] \\ & \vec{\sigma} \cdot \left[\frac{\vec{\epsilon}}{m_i + M_{P_{11}}} + \left(\frac{\vec{p_i}}{E_i + m_i} - \frac{\vec{R}}{E_{P_{11}} + M_{P_{11}}} \right) \frac{(2\vec{\mu}_1 - \vec{k}) \cdot \vec{\epsilon}}{(\mu_1 - k)^2 - m_\pi^2} \right] |\chi_i\rangle \end{aligned} \tag{9}$$

where $g^{*2}/4\pi = 10.34$ is related to the πN partial width through

$$\Gamma_{\pi N} = \frac{3g^{*2}}{4\pi} \frac{q^{*3}}{M_{P_{11}}(E_f + m_f)}$$

One recognizes, in the last bracket of Eq. 9, the contact term (proportional to $\vec{\sigma} \cdot \vec{\epsilon}$) and the pion exchange term.

3 Unitarity

Adding a resonant contribution to a non resonant (real) background violates unitarity. While methods to restore unitarity are well known [13] when one resonance dominates and when only one channel is open, the game becomes more tricky when several channels are open. Near threshold, where a few partial waves contribute and/or a few channels are open, a coupled channel approach may prove to be a useful guide to analyze the data. This is almost impossible at high energies where more channels are open. There approximate methods should be used, the most popular of which is the Eikonal Absorption Model [14].

This model assumes that after being produced through the Born terms the pion and the A, or the emitted resonance, scatter without being deviated. The only effect is a lost of flux due to the coupling to other open channels, which suppresses the Born term contribution. Each partial wave should then be multiplied by an absorptive factor which is related to the imaginary part of the corresponding elastic scattering phase shift, and eventually to the reaction cross-section and the slope of the elastic scattering angular distribution at forward angle.

Since we are interested in understanding the main trend of the data in a wide energy range, this is the method which we have retained. We leave for a later publication a coupled channel treatment more appropriate to the threshold region.

Accordingly with the analysis of Lüke and Söding [4], we have multiplied the contact Born terms, each leading to a unique spin final state ($J=\frac{3}{2}$ for the $\pi\Delta$ channel for instance), by the asymptotic expression:

$$S_{ff}^{1/2} = \sqrt{1 - \xi_\Delta exp[-(J-1/2)^2/2A_\Delta R^{*2}]}$$

where $\xi_\Delta = 1$, A_A=8 GeV^2, and R^* is the momentum of the recoiling resonance in the overall cm. frame. Initial state absorption effects have also been taken into account above the ρ production threshold, according to the vector dominance model, through the multiplicative factor :

$$S_{ii}^{1/2} = \sqrt{1 - \xi_\rho exp[-(J-1/2)^2/2A_\rho q_\rho^2]}$$

with ξ_ρ=1, and A_ρ=5.5 GeV^2. The momentum of the ρ, in the overall c.m. frame, is q_ρ^2.

Since the pion exchange graphs (fig.1-IB, and IVB) project out on many partial *waves,* they ought to be evaluated singly before applying the absorptive corrections. To simplify the resulting calculations, thereby avoiding a multipole expansion, we found it more convenient to multiply the pion exchange terms by a dipole form factor with a 900 MeV cut-off mass.

4 Comparison with experiment

4.1 The high energy sector of the $p\pi^+\pi^-$ channel

As is clearly demonstrated on Fig. 2, the absorptive corrections significantly reduce the Born cross-section and restore the agreement with the measured values of the $\Delta^{++}\pi^-$ cross section in the energy range $2 < E_\gamma \leq 5$ GeV. The $\pi\Delta$ contact term, which dominates at low energy, is almost completely suppressed above $E_\gamma \simeq 2$ GeV, where the pion exchange Born term dominates. At high energy, the ρ diffractive production mechanism accounts for the strength in the $\gamma p \to \rho p$ channels. Below $E_\gamma = 2$ GeV, the excess of experimental cross-section indicates the need to include higher mass, and strongly decaying into the ρ channel, resonances than those taken into account in the present study.

We find also that, above $E_\gamma = 1$ GeV, the πP_{11} and πD_{13} Born terms contribute significantly to the cross section of the full $\pi^+\pi^-$ charnel. They, however, do not exhibit the proper high energy behavior since our model clearly overestimates the data above $E_\gamma = 2$ GeV. On the other hand, both the Δ^{++} and ρ production channels are correctly reproduced. Therefore, following the recipe described in the appendix, we have replaced the usual pion exchange amplitudes by Regge Pole exchange amplitudes which are known to exhibit the correct high energy behavior. Fig. 3 shows the marked improvement in the description of the data at high energy after this modification has been applied. In the following discussion, we only make use of the results of the modified model. We leave to a later paper a more comprehensive study of the implications of Regge phenomenology.

Figs. 4 and 5 show respectively $p\pi^+$ and $\pi^+\pi^-$ mass spectra at $E_\gamma = 1$ and 3 GeV. The model agrees fairly well with the normalized data from ref [1]. The Δ^{++} and the ρ clearly appear. On fig.4, the excess of experimental cross-section in the $p\pi^+$ spectrum, around 2 GeV, strongly suggests some contributions from Born Terms associated with A resonance in this mass range.

Fig. 6 shows the double differential cross-section $d\sigma/dM_{p\pi^+}dt$ at $E_\gamma = 5$ GeV. The four-momentum transfer, between the incoming photon and the outgoing π^-, is $t = (k - \mu_1)$. In the t distribution, the direct A^{++} contribution (Fig.1.I) appears clearly above that of the background due to the other processes.

We next applied a cut on the mass distribution of fig. 6 in order to concentrate on the contribution from the A++. This cut corresponds to $1170 \leq M_{p\pi^+} \leq 1400$ MeV. Fig. 7 shows the results from this operation and allows us to compare the resulting distribution with the experimental data available at $E_\gamma = 5$ GeV. We note that the A^{++} contribution decreases quickly with increasing t, as is expected, but that above $-t \simeq 2$ GeV^2 the $p\pi^+$ background dominates becoming comparable to the experimental data. It should be noted, however, that this experiment [15] was

performed with a continuous Bremsstrahlung beam and the Δ^{++} really couldn't be reliably identified. We suggest that this experiment should be repeated using the intense monochromatic real photon beam soon to be made available at CEBAF.

4.2 The low energy sector

We now compare the predictions of our model with most of the available experimental data obtained at energies up to E_γ=1 GeV, and in particular with the recent high quality data from Daphne. This is the domain where meson exchange models are expected to be more valid and where absorptive corrections should not dominate.

4.2.1 The $p\pi^+\pi^-$ Channel

In this reaction channel, every mechanism, except the direct ρ production (fig.1-V), is present. We find, as shown on fig.8, that more than half of the cross-section, as well as the overall shape, are explained by the presence of the $\pi\Delta$ born term (fig.1-I). Both the $\Delta^{++}\pi^-$ and the $\Delta^0\pi^+$ intermediate states have been explicitly calculated. Around E_γ=600 MeV, the remainder of the cross section is essentially due to the interference of the $D_{13}(1520)$ resonance in the s-channel with the contact part of the $\pi\Delta$ Born term. Around E_γ = 900 MeV, the additional shoulder showing up in the cross section is due to interference of the $D_{33}(1700)$ resonance with the Born term. Contributions from the other mechanisms shown in fig.1, though small, have also been explicitly included.

Our results, using the central value of parameters extracted from the analysis of other experiments [8], are in good accord with the Daphne data. A better fit to the cross-section could have been obtained by slight adjustment of some of the parameters, within their error bars, but we stress again that this is not the object of this paper.

4.2.2 The $p\pi^0\pi^0$ Channel

This channel is characterized by the absence of any of the Born terms. This is due to the fact that since π^0 cannot couple to photons, graphs I-b and IV-b of fig.1 are forbidden. By gauge invariance arguments, this implies that the contact parts, graphs I-a, and IV-a, are suppressed. Finally, as the ρ may not decay into two π^0, graphs II-b, and V are also absent. This makes the $p\pi^0\pi^0$ channel ideally suited for the study of the nucleon resonances, since only graphs II-a and 111 are allowed to remain.

The calculated cross-section is shown on fig.9, along with the contribution from

the appropriate diagrams, and the experimental data obtained with Daphne. We have found that major part of the cross-section is essentially due to the presence of the $P_{11}(1440)$ resonance decaying into the σ. The parameters describing the various couplings to the σ are the same which have been obtained in the analysis of the $\pi N \rightarrow \pi\pi N$ channel [6]. One should note also the suppression of the strength of the $D_{33}(1700)$ due to the isospin coupling constant. Finally, Fig. 10 shows the mass spectra of the two emitted neutral pions as well as of the $p\pi^0$ pair at photon energies of 1 and 3 GeV. The contributions of the A and σ emission channels are clearly separated, especially at the higher energy.

4.2.3 The $n\pi^+\pi^0$ Channel

This last channel turns out to be the most difficult to interpret, as it contains subtle aspects of the previous two. Half of the Born terms are present, since only the charged pion can couple to the photon. Graphs Ia,b and IVa,b must, therefore, be calculated for the $\Delta^0\pi^+$ channel only. The only graph which is totally absent is III-b, which, for this channel, violates charge conservation. The results of our calculations are shown on fig.11, along with the data obtained with Daphne, and the contribution from the more important mechanisms. Every known resonance which could contribute in the energy range under consideration has been included. There are still no free parameters involved.

Fig.12 shows a comparison of our model with data obtained on the reaction $\gamma n \rightarrow p\pi^-\pi^0$, which is the isobaric mirror of reaction presently being discussed. While in the Daphne energy range the model greatly underestimates the experimental data, it is encouraging to note that for energies above 1 GeV it does reproduce the data quite well, in spite of not having included Fermi motion effect in the originally measured $\gamma D \rightarrow \pi^-\pi^0 pp$ reaction cross-section. One should note the sizable contribution of the p production contact term. Its shape reflects the manner in which we have implemented absorption in the p channel, namely no absorption below the p production threshold.

For completeness, the mass spectra of the emitted $\pi^-\pi^0$ pair are shown on Fig.13 at photon energies of 1 and 3 GeV. The contribution of the p production channel appears clearly.

4.2.4 Discussion and prospects

This discrepancy in the $n\pi^+\pi^0$ channel between the experimental results and the model is disconcerting and calls for improvements. On the one hand, there is a high level of confidence in the experimental data [3]. On the other hand, the good agreement for the other two channels does not allow much freedom in the present

version of the model. Two improvements are worth considering.

We suspect that the manner in which we have dealt with unitarity, while correct at high energies, might not be appropriate in the Daphne energy range. Though it takes correctly into account the loss of flux of the emitted particles, due to the coupling to the other open channels, it does not deal correctly with the addition of a resonant contribution to the Born background, nor with possible increase of the cross-section due to charge exchange rescattering mechanisms. A complete implementation of unitarity, in a full coupled channel approach, seems to be the way to proceed but lies outside the scope of this paper.

The second improvement will be to include the contributions of higher mass resonances, both in the s-channel and the Born Terms, and to play with their parameters in the limits of the range allowed by the analysis of other experiments. However, before playing such a game, the prerequisite is to master the non resonant background and to know how to add resonant contributions in a unitary way.

These issues, as well as the effects of other speculative mechanisms, will be addressed at a later time.

5 Conclusion

By improving the model of Lüke and Söding, we have reproduced the $p\pi^+\pi^-$ data to an acceptable level. At low energy, we do agree with the older premise that most of the cross-section is due to the presence of the $\Delta\pi$ born term, and especially its contact part. Effects of the $D_{13}(1520)$ are also evident by interference with the contact part of the Born term. We have shown, in addition, the contribution of the $D_{33}(1700)$, which also interferes with the Born term. Finally, the contributions of the Born terms associated with the πP_{11} and πD_{13} channels become more important as the energy increases.

Our most important result lies in our analysis of the $p\pi^0\pi^0$ data. The good agreement between our model and the experiment is of its own accord extremely interesting. It shows clearly, for the fist time, a direct evidence for the production of the $P_{11}(1440)$ resonance by real photons. This is an important result in view of understanding the nature of the P_{11} (1440) which, in the naive quark constituent model, is thought to be the radial excitation of the nucleon. Our results tend to be in conflict with this simplest representation as real transverse photons may not excite such a mode. This indicates a more complicated structure. We have also shown that this resonance manifests itself through its strong decay into two π^0, in a relative S-state, as parameterized by the σ meson.

At low energies, the discrepancy between the model and a recent accurate mea-

surement of the $\gamma p \to n \pi^+ \pi^0$ reaction cross-section calls for a more involved treatment of unitarity.

When extended to higher energies, this meson exchange model provides us with a fair accounting of the trends of the experimental data. However, a description based on the exchange of Regge trajectories is more appropriate. A full implementation of Regge phenomenology will be the matter of a next paper.

Nevertheless, the present version of the model provides us already with a good starting point to simulate experiments planned at existing facilities such as CEBAF.

Appendix

When extrapolated at high energies, meson exchange Born amplitudes are known to lead to the wrong energy (W) as well as transfer momentum ($-t$) dependence of the corresponding cross-sections, which often violate unitarity bounds. Regge Pole Exchange phenomenology offers us with a powerful way to extrapolate far from meson poles, while satisfying unitary constraints at high energies (see for instance Ref [16]).

Accordingly with Ref. [17], we have replaced the pion propagator, in Eq. 8 and Eq. 9, by the corresponding Regge amplitude :

$$\frac{1}{t - m_\pi^2} \to \frac{1}{\Gamma(\alpha+1)} \left(\frac{s}{s_o}\right)^\alpha \frac{\pi\alpha'}{2} \frac{1 + e^{-i\pi\alpha}}{\sin \pi\alpha} \tag{A.1}$$

where $s = W^2$ is the total c.m. energy squared, $s_o = 1$ GeV, and $\Gamma(\alpha)$ is the Gamma function.

The Regge trajectory is defined as :

$$\alpha \equiv \alpha(t) = \alpha'[t - m_\pi^2] \tag{A.2}$$

with $\alpha' = 0.7$ GeV-a.

It is easy to verify that this Regge amplitude does coincide with the pole amplitude $1/(t - m_\pi^2)$, near the pole as $t + m_\pi^2$.

References

[1] ABBHHM Collaboration, *Phys. Rev.* 175 (1968) 1669.

[2] G. Gialanella , *et al, Nuovo Cimento* **63A** (1969) 892.

[3] A. Bragheri, L.Y. Murphy, *et al, Phys. Lett.* **B363** *(1995) 46.*

[4] D. Lüke and P. Söding, *Springer Tracts in Modern Physics* 59 (1971) 39.

[5] J.A. Gomez-Tejedor and E. Oset, *Nucl. Phys.* **A571** (1994) 667.

[6] D.M. Manley *et al., Phys. Rev.* **D45** (1992) 4002.

(7] R.A. Arndt *et al., Phys. Rev.* **D42** (1990) 1864;
Zhujun Li *et* al., *Phys. Rev.* **C47** *(1993) 2759.*

[8] Particle Data Group, *Phys. Rev.* **D50** (1994) 1173.

[9] J.M. Laget, *Phys. Rep. 69 (1981) 1,* and references therein.

[10] I. Blomquist and J.M. Laget, *Nucl. Phys.* **A280** *(1977) 405.*

[11] R. Machleidt, K. Holinde, Ch. Elster *Phys. Rep.* **149** (1987) 1.

[12] J.M. Laget and R. Mendez-Galain *Nucl. Phys.* **A581** (1995) 395.

[13] M.G. Olsson, *Nucl. Phys.* 1378 (1974) 55;
R. Davidson *et al., Phys. Rev. Left.* 56 (1986) 804.

[14] J.D. Jackson, *Rev. Mod. Phys.* 37 (1965) 484;
K. Gottfried and J.D. Jackson, *Nuovo Cimento* 34 (1964) 735.

[15] R.L. Anderson *et al., Phys. Rev.* **D14** (1976) 679.

[16] P.D.B. Collins and A.D. Martin *Hadron Interactions* Adam Hilger Ltd 1984.

(17] N. Levy *et al. Nucl. Phys.* **B55** (1973) 493.

Figure Captions.

Fig.1 : The graphs considered in the present model.

Fig.2 : Plots of the $\gamma p \to \Delta^{++}\pi^-$, $\gamma p \to \rho p$ (top) and $\gamma p \to p\pi^+\pi^-$ (bottom) cross-sections from threshold up to 5 GeV. In the top part, the results from the complete model are shown by the solid line. The Born term (fig.1-I) is the hashed curve. We show also, by the dot-dashed curve, the total $\Delta^{++}\pi^-$ cross section when the absorptive corrections are turned off. The dotted curve corresponds to the contribution of diffractive ρ production. In the bottom plot, the results from the complete model are displayed with and without the diffractive ρ production by the dot-dashed and dashed curve respectively. The complete $\Delta^{++}\pi^-$ channel is once again described by the solid curve. Finally, the D_{13} and the P_{11} Born terms (fig.l-IV) are shown respectively as the dotted and dot-dashed curve. The experimental data are from Ref. [1] : A^{++}(o), ρ (o) and full $\pi^+\pi^-$ (A) channels.

Fig.3 : The full curve shows the effects of the Reggeization of the pion exchange P_{11} and D_{13} Born Term on the total cross-section of the $\pi^+\pi^-$ channel. The dash-dotted curve shows the results of the meson exchange model (as in Fig. 2), while the dashed curve shows the contribution of the A^{++} emission channel.

Fig.4 : The $p\pi^+$ mass spectrum in the reaction $\gamma p \to p\pi^+\pi^-$ at E_γ = 1 and 3 GeV. The experimental data come from Ref. [1).

Fig.5 : The $\pi^-\pi^+$ mass spectrum in the reaction $\gamma p \to p\pi^+\pi^-$ at E_γ = 1 and 3 GeV. The experimental data come from Ref. [1].

Fig.6 : The momentum dependence of the $p\pi^+$ mass spectrum in the reaction $\gamma p + p\pi^+\pi$ - at E_γ = 5 GeV.

Fig.7 : The full histogram shows the momentum dependence of π^- emitted in the reaction $\gamma p + \Delta^{++}\pi^-$ at E_γ = 5 GeV. The dashed histogram represents the contribution of the background below the A^{++} peak in the mass range 1170< $M_{p\pi^+} \leq$ 1400 MeV. The experimental data come from Ref. [15]. The rise of experiment at large t indicates a possible contribution of graph Ic which is not included in this calculation.

Fig.8 : The cross-section of the $\gamma p \to p\pi^+\pi^-$ channel below E_γ = 1.1 GeV. The complete model is shown on the top part of the figure by the solid line. The contribution from the Born term (fig.1-I), the D_{13} and the P_{11} Born terms (fig.1-IV) are, respectively, the dotted line, the long dashed and the long dot-dashed curves. The dashed curve, the dot-dashed, and the closely spaced dotted curves display the results obtained with the Born+D_{13}, the Born+D_{33} and the Born+D_{13}+D_{33} alone, showing clearly the interference between these terms. The other, lesser, contributions are shown on the bottom part of the figure. The P_{11} graphs described by fig.1-IIIa, and IIIb are the solid, and dot-dashed lines. The D_{13} graphs fig.1-IIa, and

b, are the dotted, and dashed lines. The D_{33}, depicted in fig.1-IIa, is the hashed line. The experimental data are from Refs.[1](△),[2](o), and [3] (•).

Fig.9 : The cross-section of the $\gamma p \to p\pi^0\pi^0$ channel below E_γ = 1.1 GeV. 'The total cross section is plotted as the solid curve. The D_{13}, and the D_{33} contributions (fig.1-IIa) are, respectively, the short and long-dotted curves. The P_{11} graphs from fig.1-IIIa, and IIIb are the dot-dashed, and dashed curves. The data is from Ref. [3].

Fig.10 : The $\pi^\circ\pi^\circ$ mass spectrum in the reaction $\gamma p \to p\pi^\circ\pi^\circ$ at E_γ = 700 MeV (a) and E_γ = 3 GeV (b). The contribution of the σ production channel is the dashed histogram.

Fig.11 : The cross-section of the $\gamma p \to n\pi^0\pi^+$ channel below E_γ = 1.1 GeV. On the top part, the results describing the complete model are shown by the solid line. The contribution from the Born term (fig.1-I) is the dotted line. The D_{13}, and the P_{11} Born terms (fig.1-IV) are the dashed and the dot-dashed curves. ρ production (fig.1-V) is shown by the hashed line. On the bottom part, the other contributions are plotted. The P_{11} from fig. 1-IIIa is the solid curve. The D_{13} and D_{33} graphs from fig.1-IIa are the dotted, and hashed lines. The D_{13} from fig.1-IIb is shown by the dashed line. The data is from Ref. [3].

Fig.12 : The cross section of the reaction $\gamma n \to p\pi^\circ\pi^-$ at high energy. Th$_e$ full histogram represents the result of the complete model. The dashed histogram represents the contribution of the A Born terms. The dotted and the dash-dotted histograms represent respectively the contribution of the D_{13} (including its ρ decay) and P_{11} resonances s-channel production. The cross-hatched area represents the contribution of the D_{33} resonance s-channel production (without including its ρ decay). Finally, the hatched area represents the contribution of the ρ contact term. The experimental data come from Ref. [1] (A) and Ref. [2] (.).

Fig.13 : The $\pi^-\pi^\circ$ mass spectrum in the reaction $\gamma n + p\pi^\circ\pi^-$ at E_γ = 1 and 3 GeV.

J.M. Laget, L.Y. Murphy FIG. 1

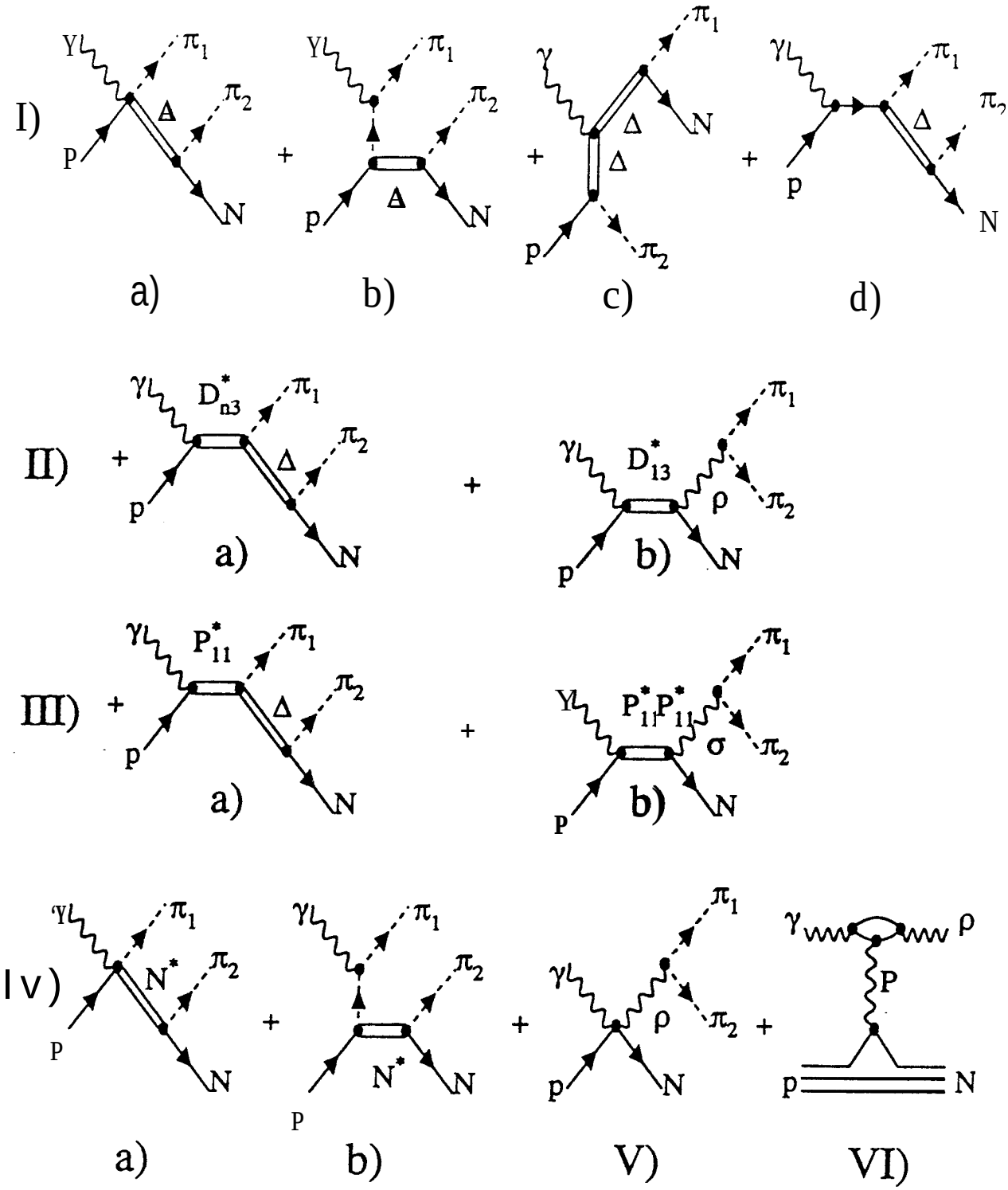

J.M. Laget, L.Y. Murphy FIG. 2

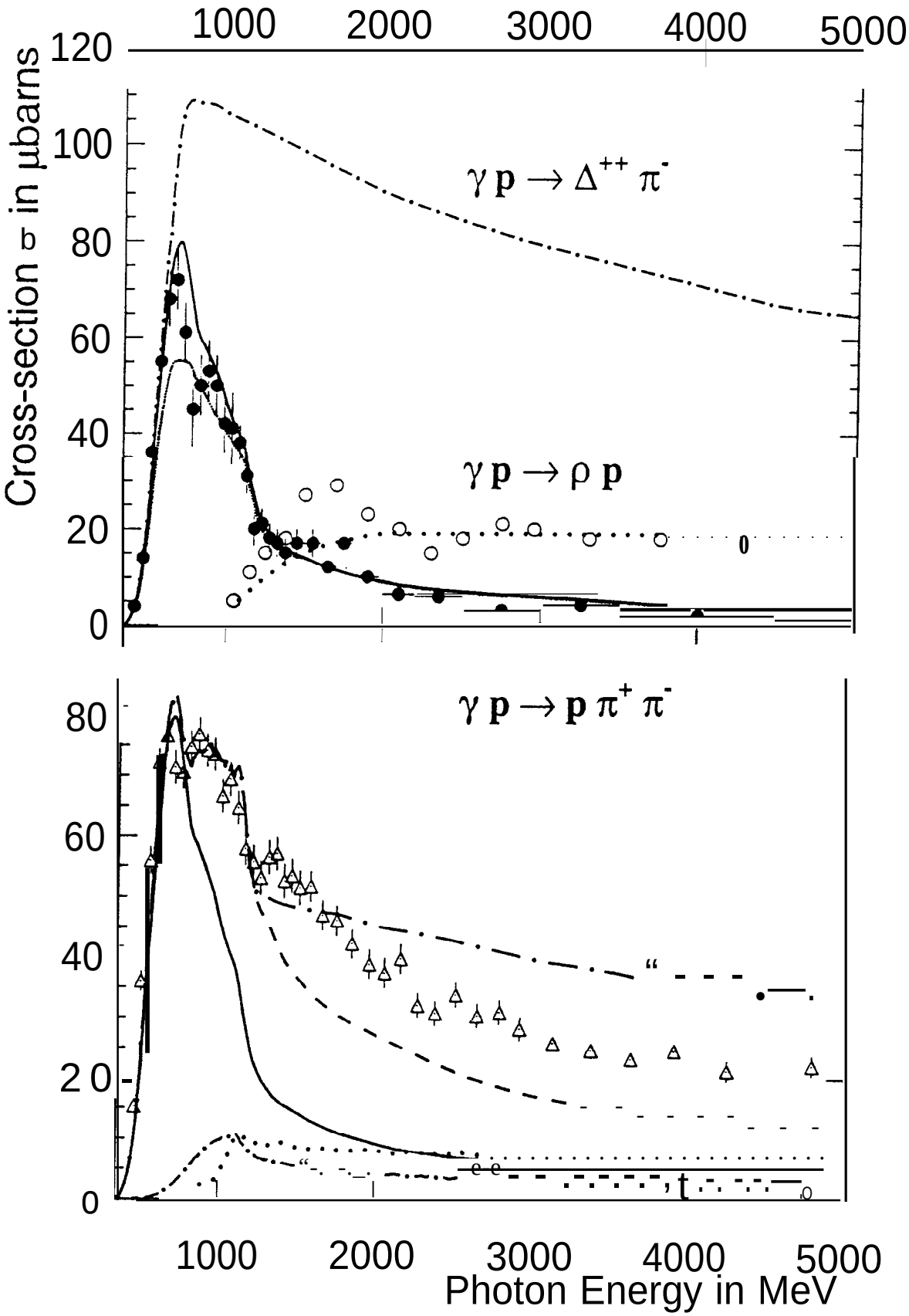

J.M. Laget, L.Y. Murphy FIG. 3

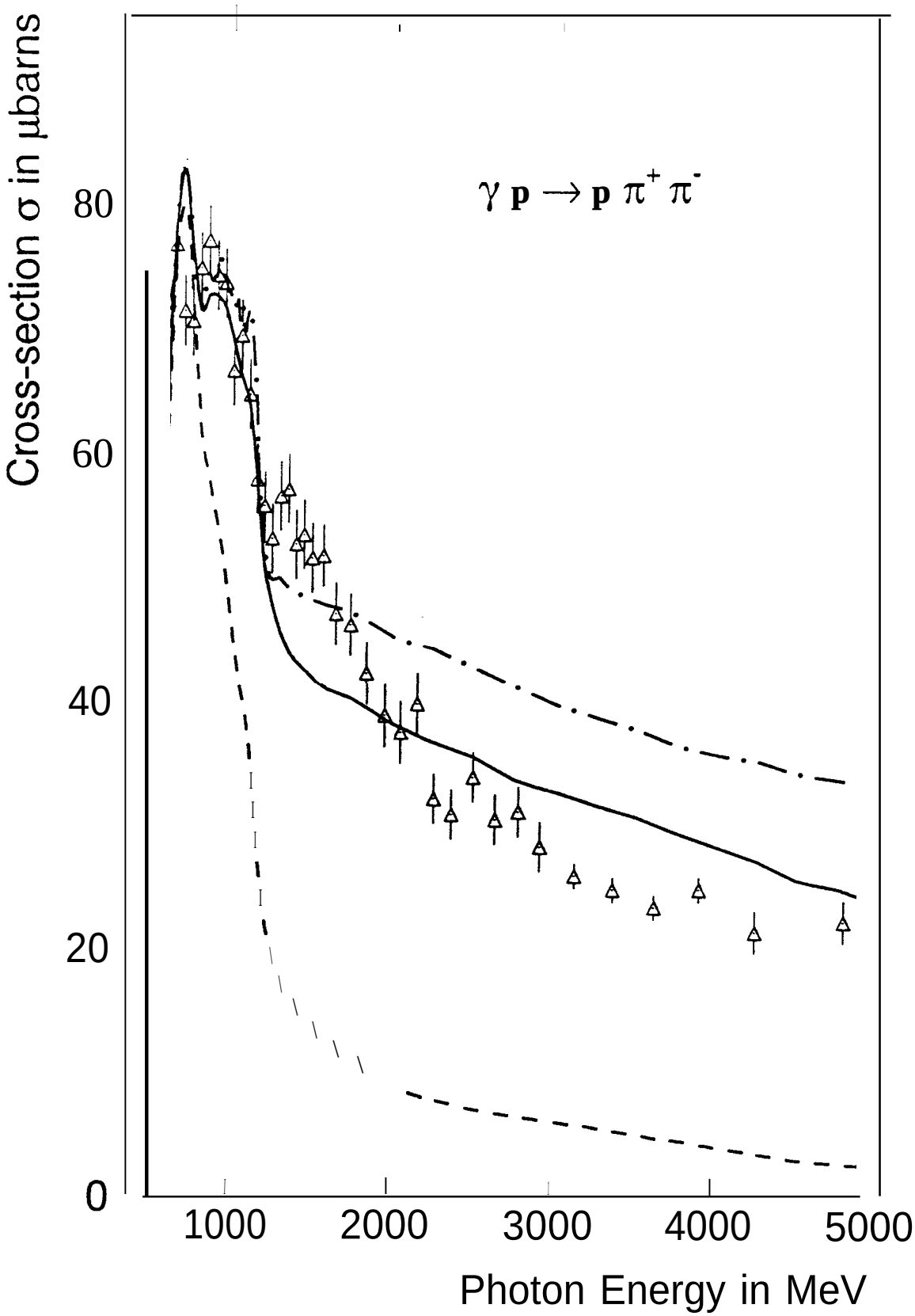

J.M. Laget, L.Y. Murphy FIG.4

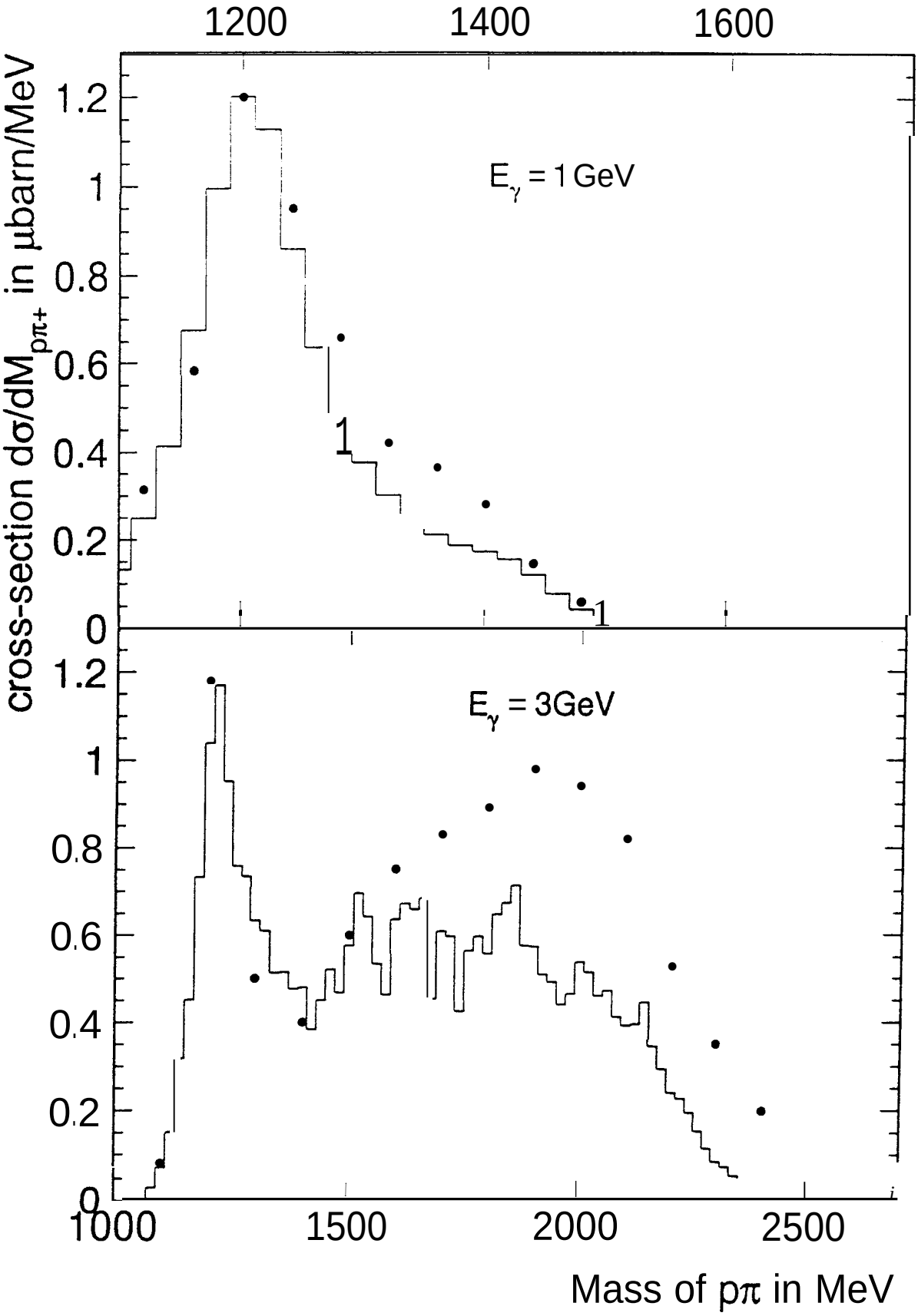

J.M. Laget, L.Y. Murphy FIG.5

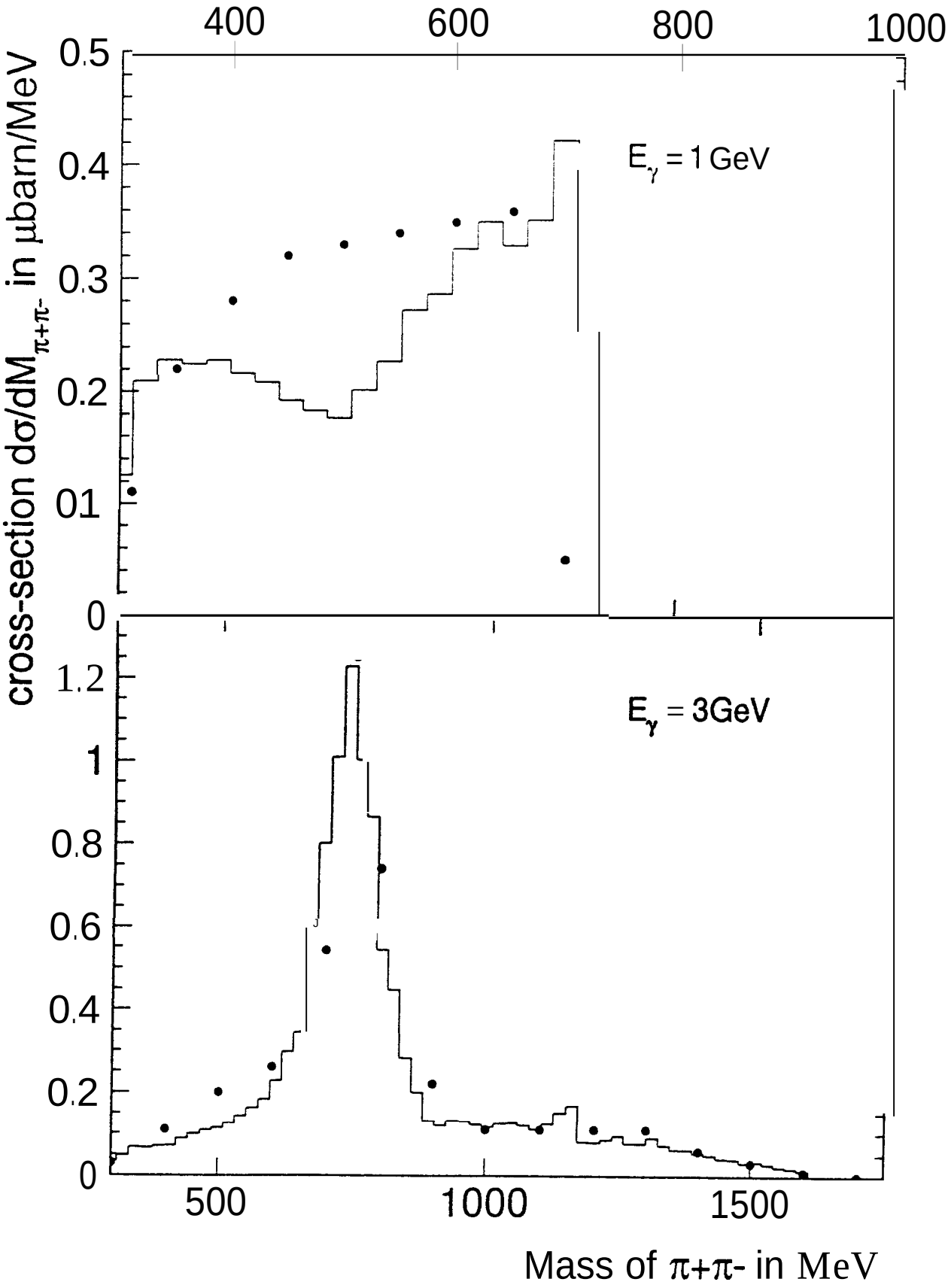

J.M. Laget, L.Y. Murphy FIG. 6

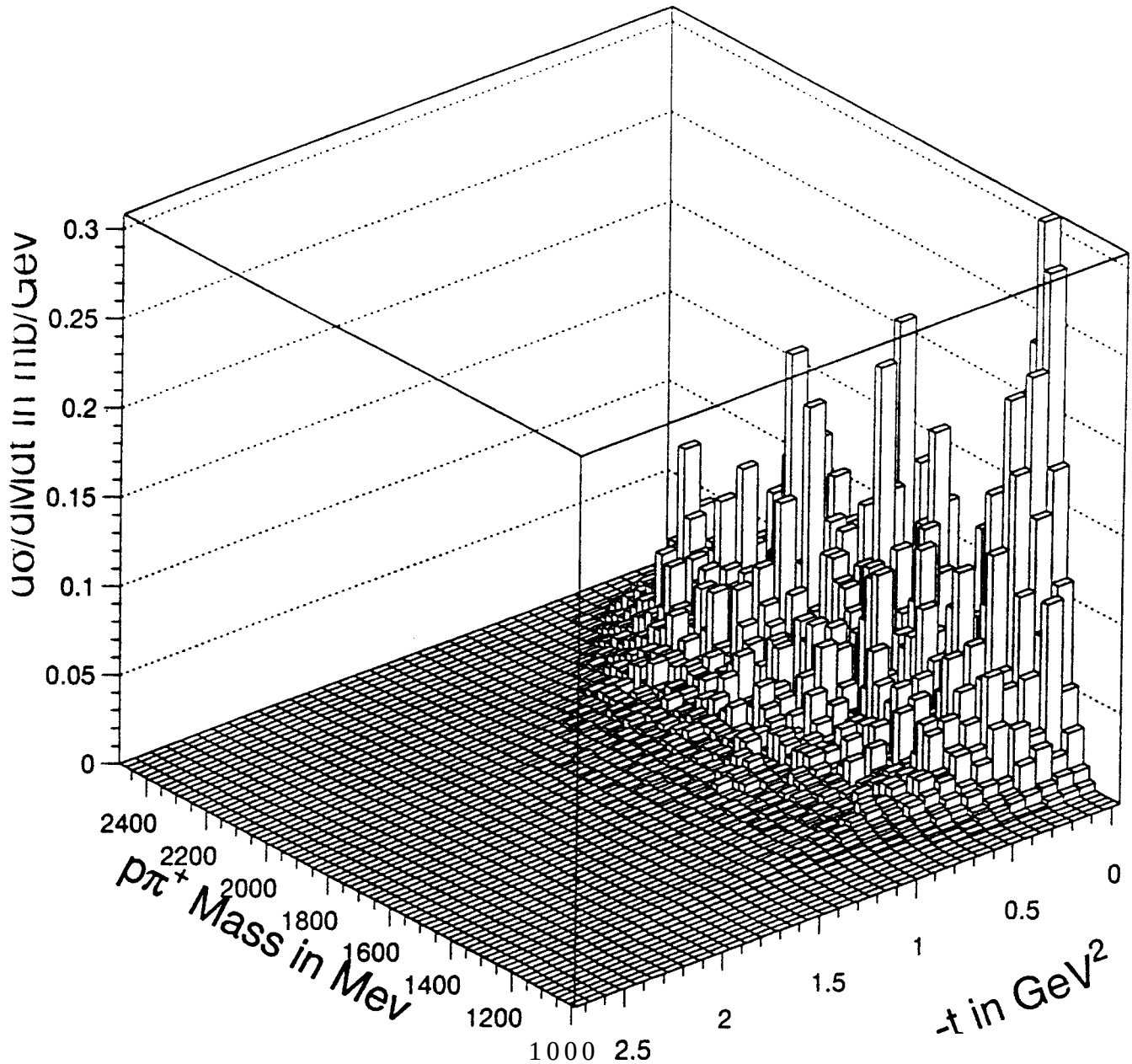

J.M. Laget, L.Y. Murphy FIG. 7

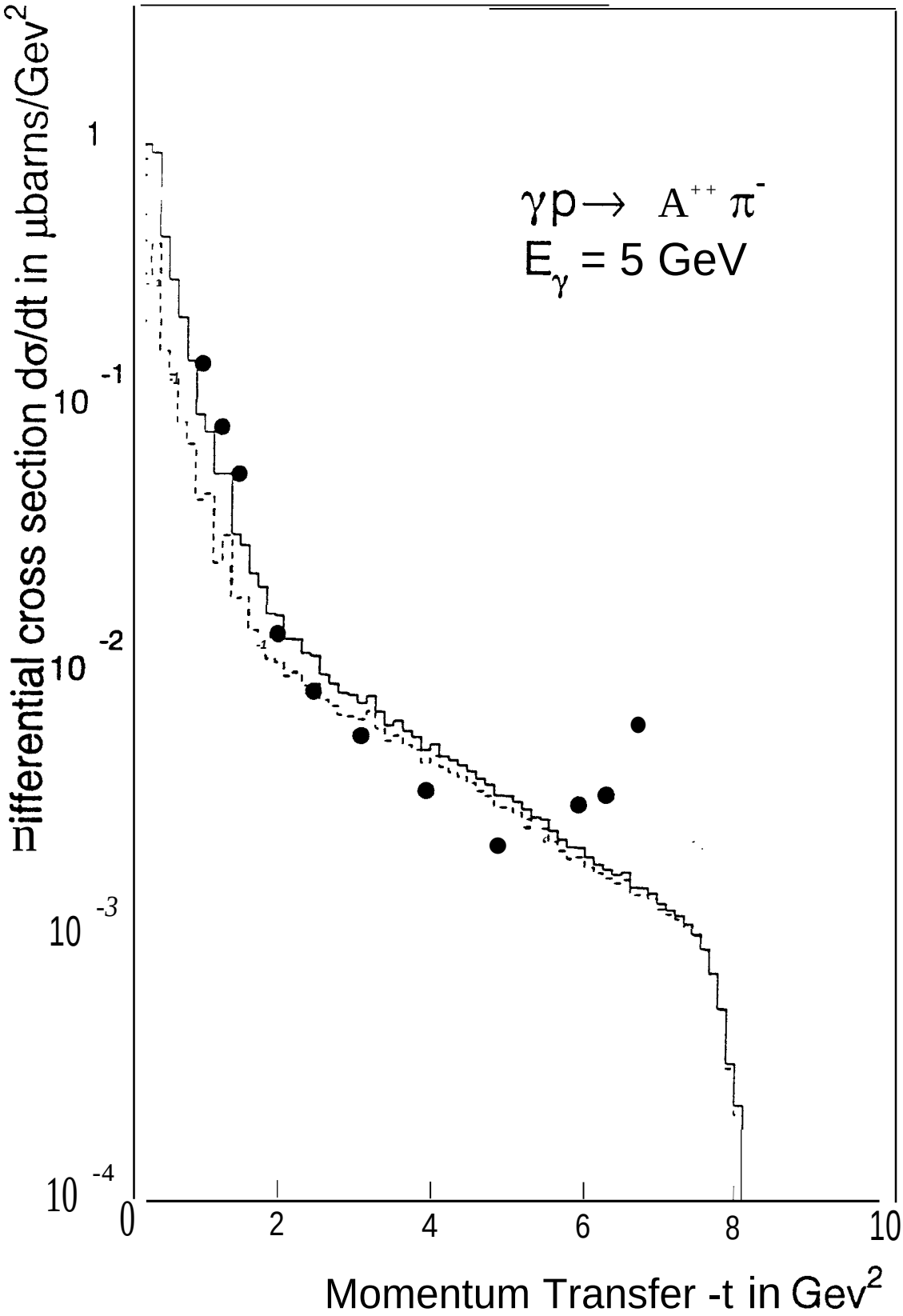

J.M. Laget, L.Y. Murphy FIG. 8

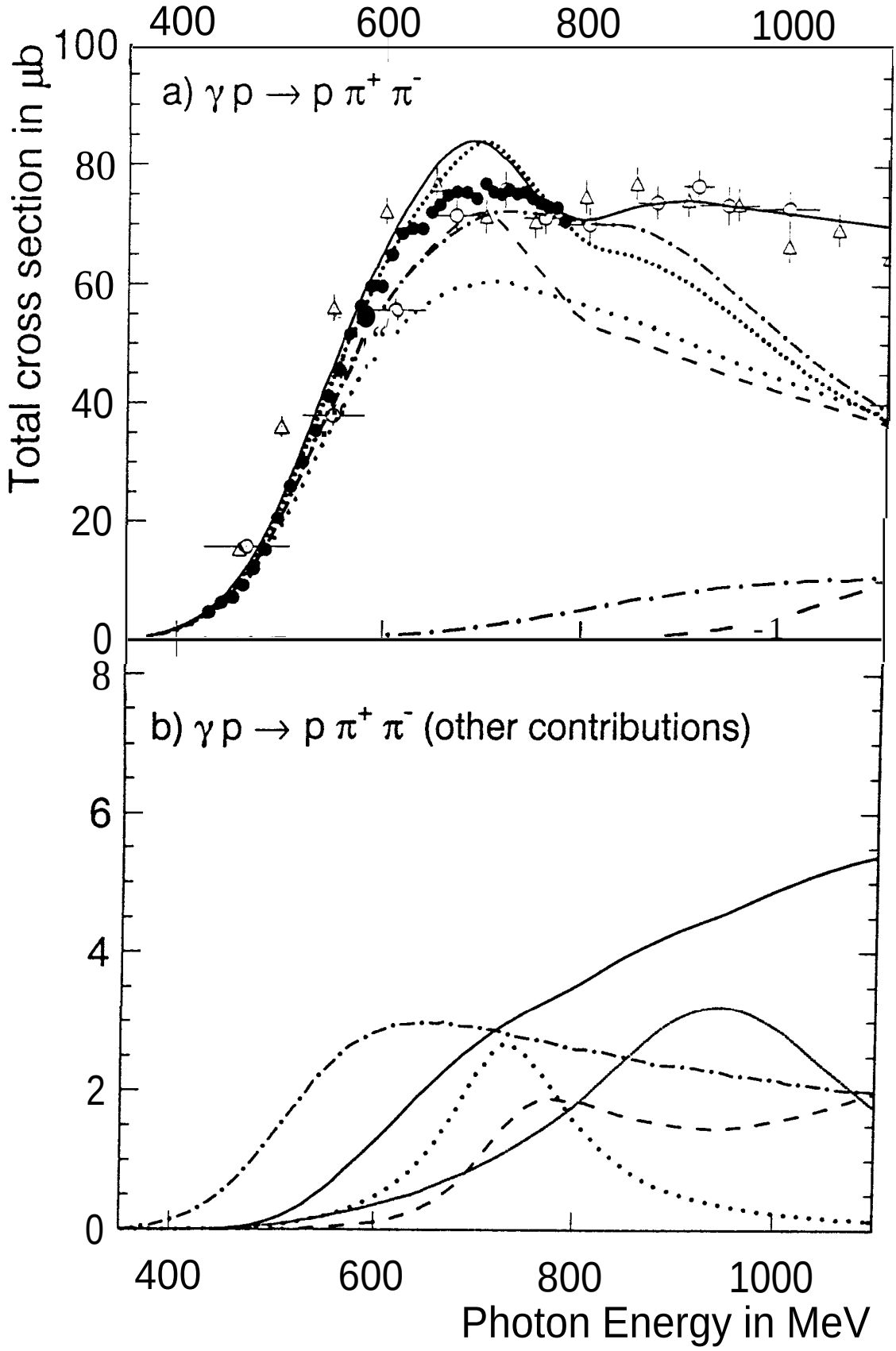

J.M. Laget, L.Y. Murphy FIG. 9

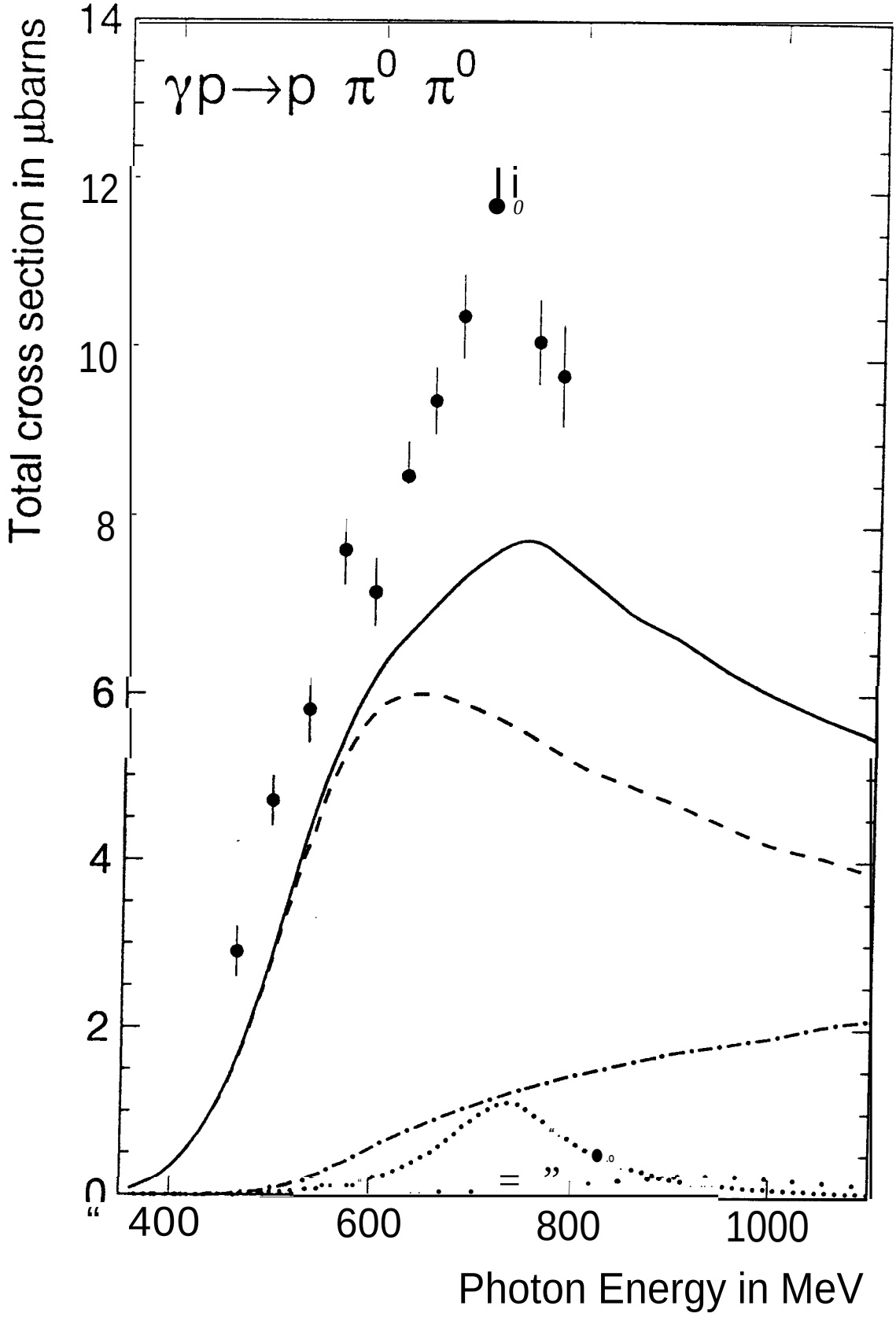

J.M. Laget, L.Y. Murphy FIG. 10a

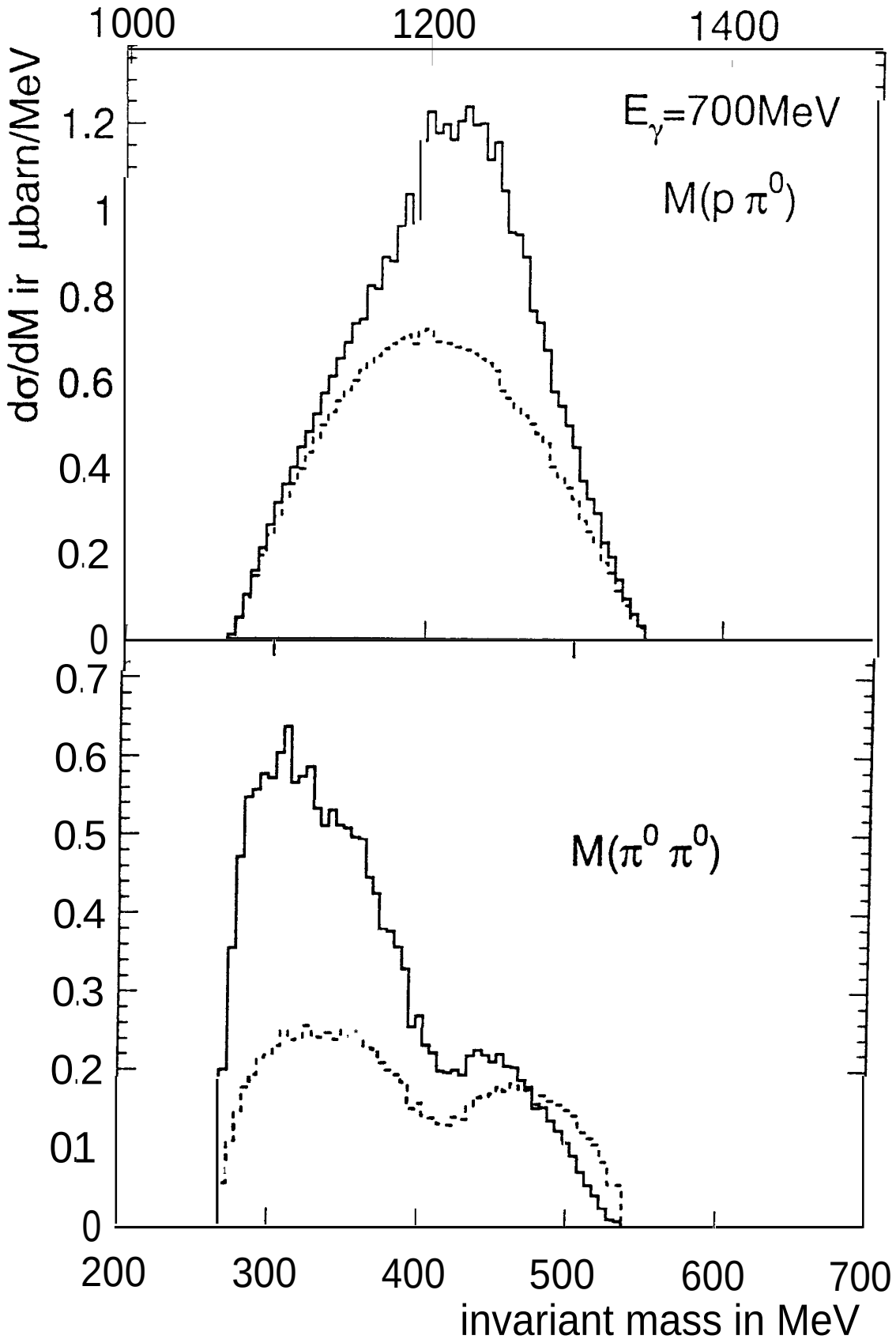

J.M. Laget, L.Y. Murphy FIG. 10b

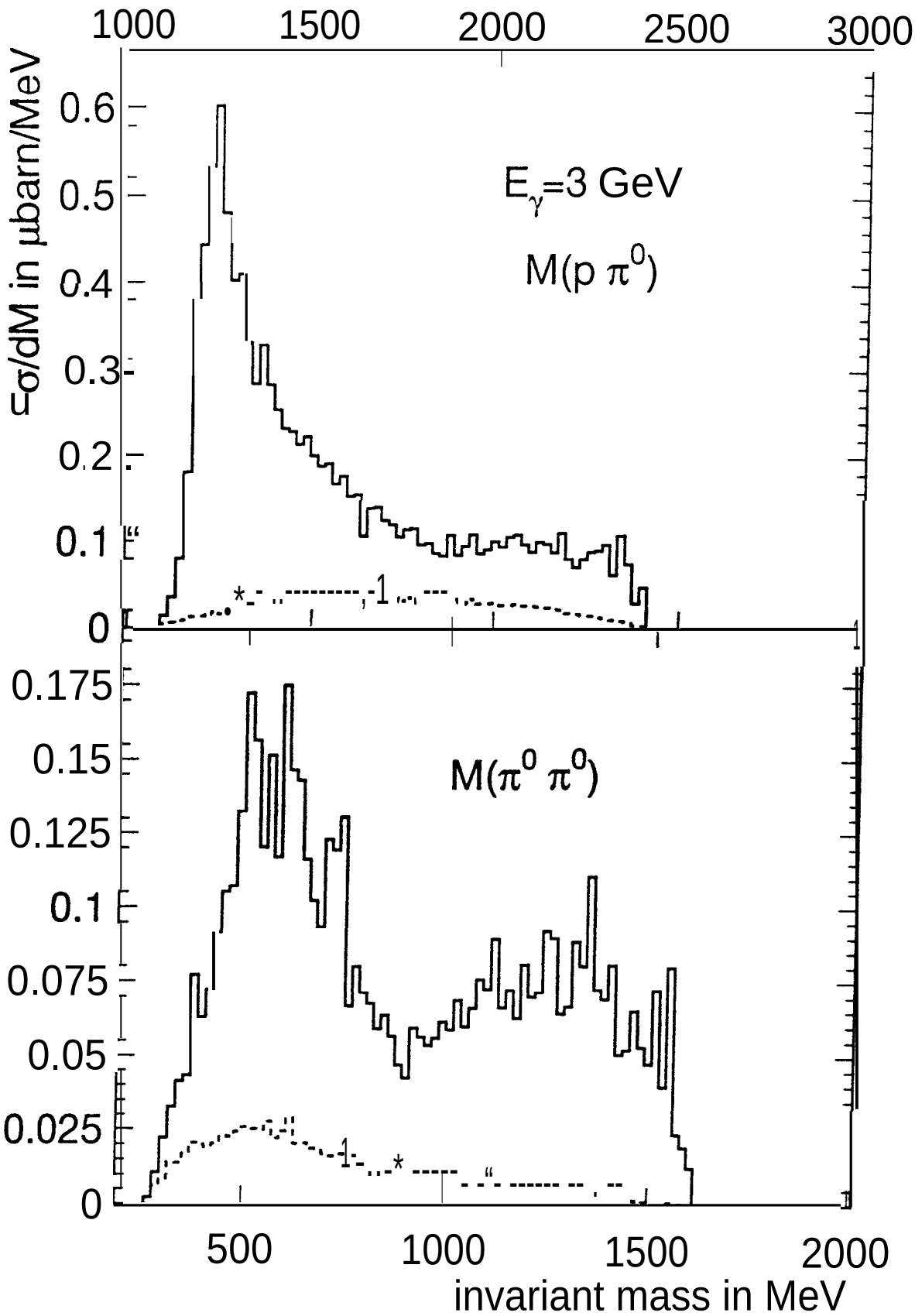

J.M. Laget, L.Y. Murphy FIG. 11

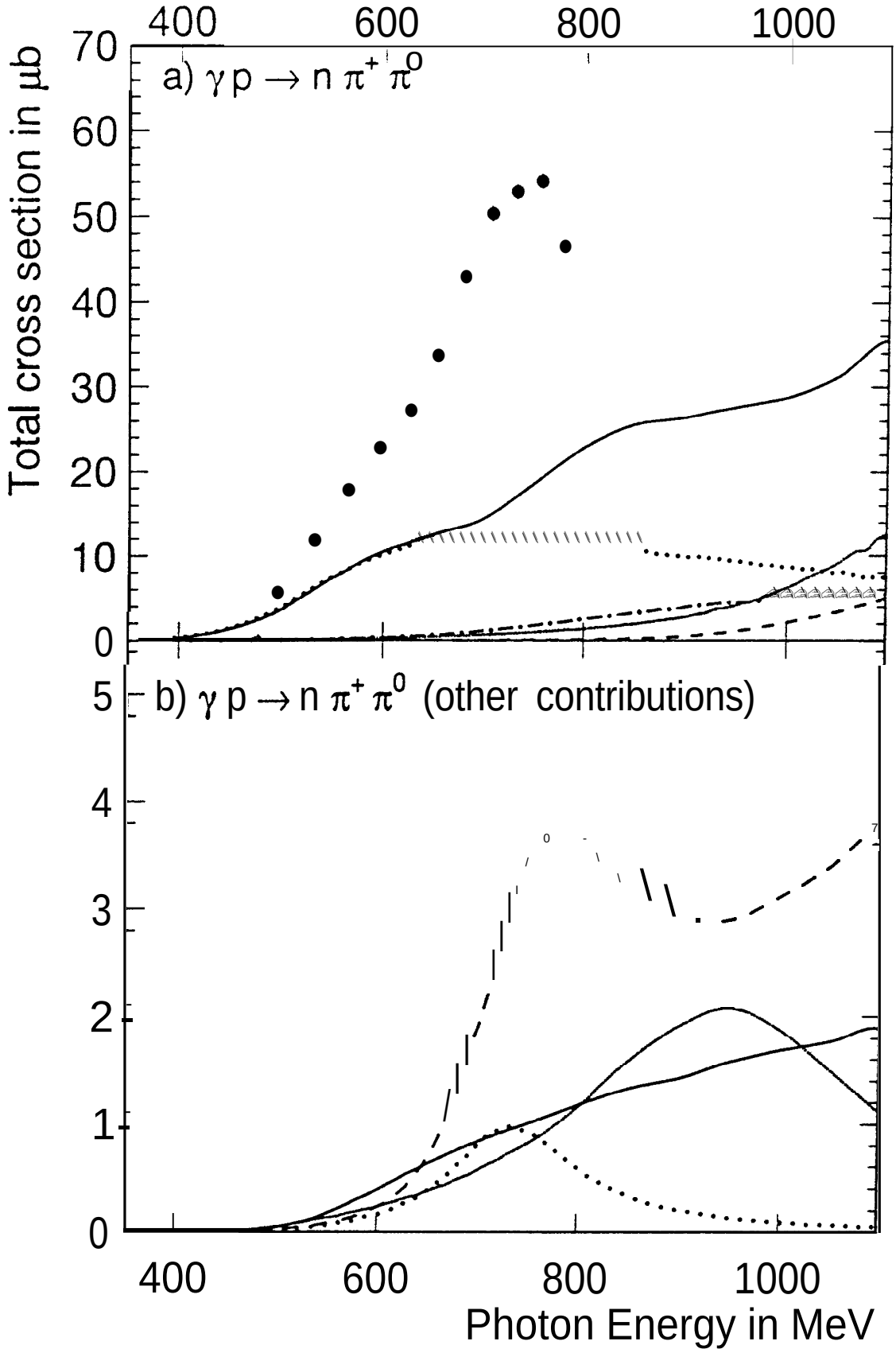

J.M. Laget, L.Y. Murphy FIG. 12

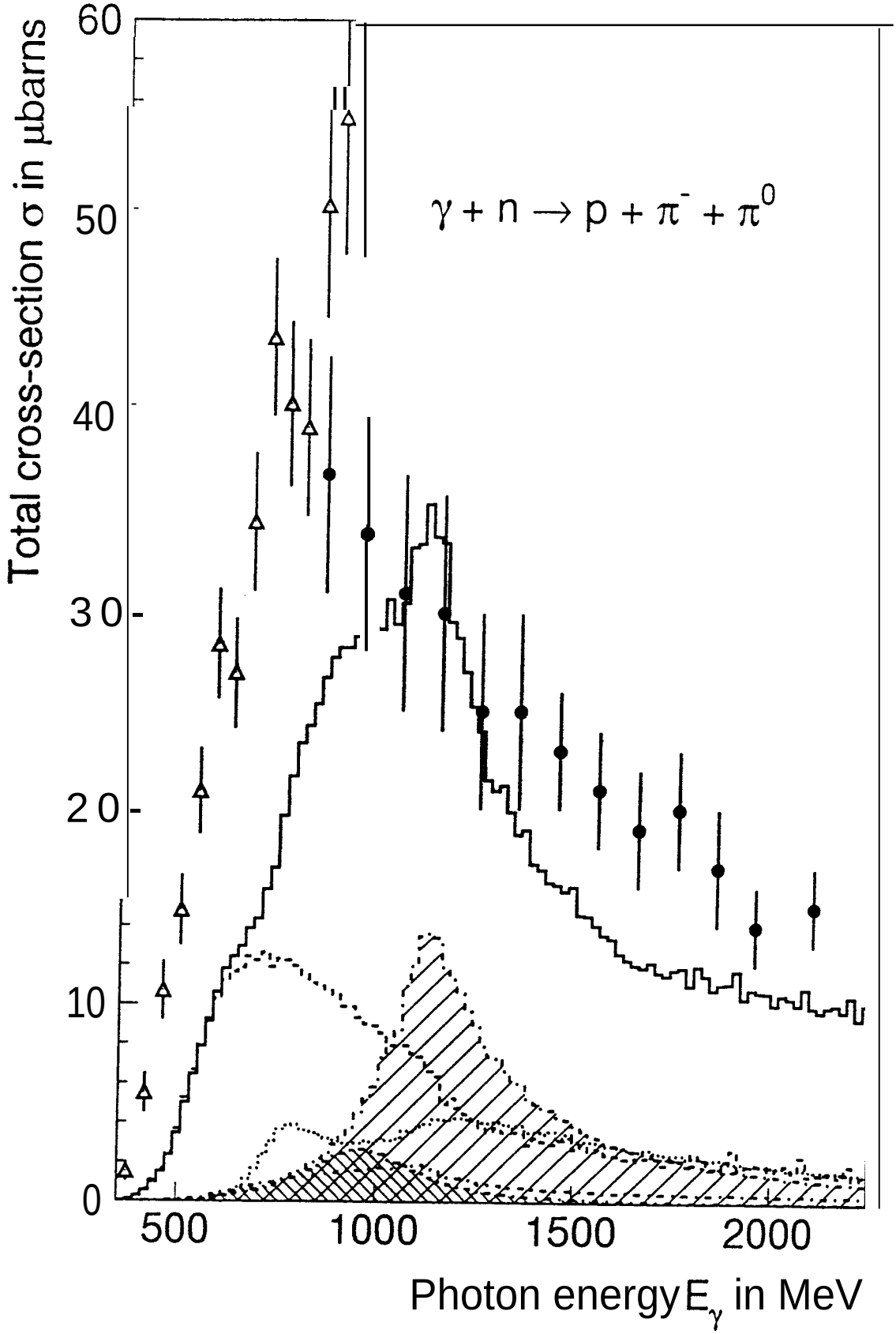

J.M. Laget, L.Y. Murphy FIG. 13

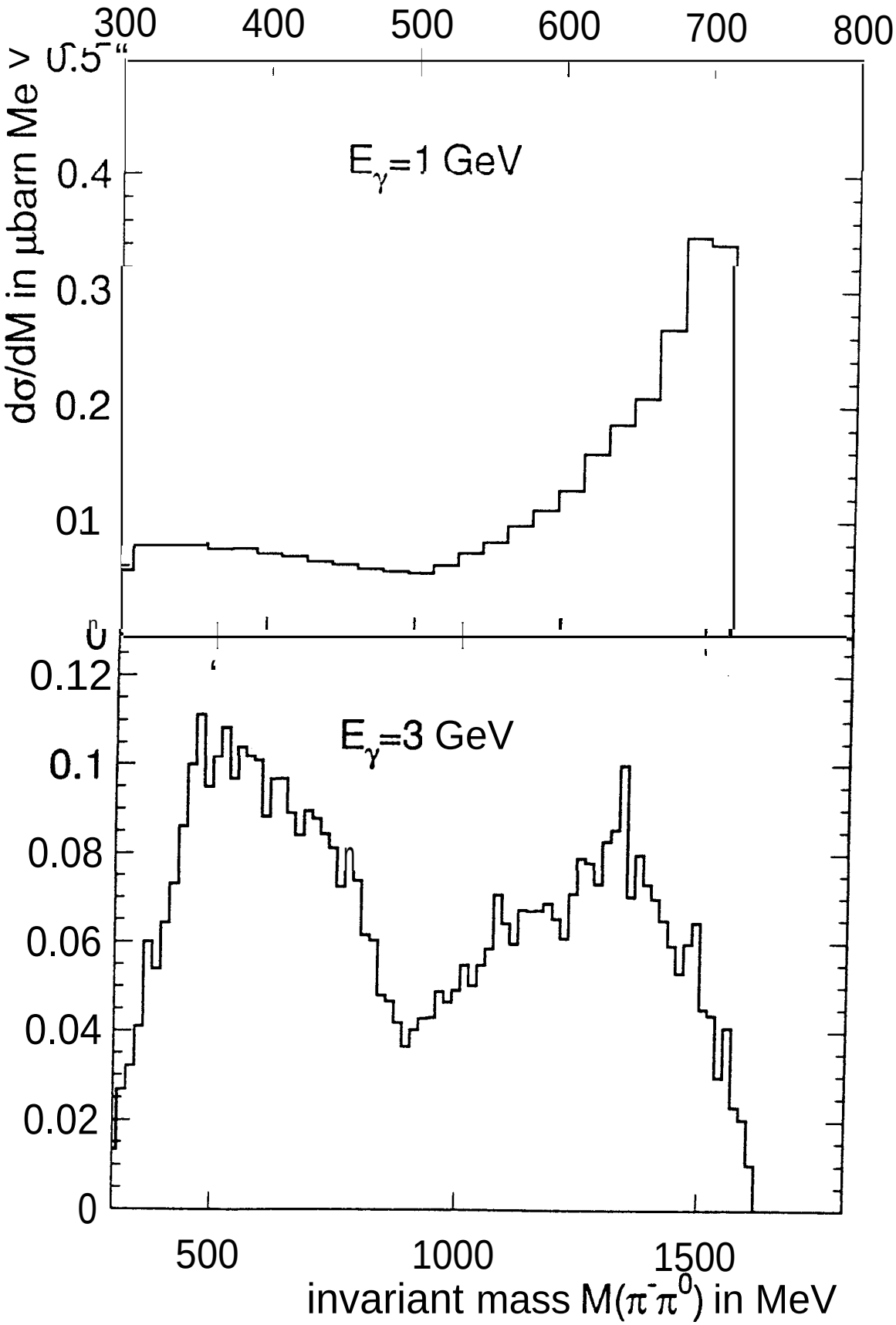

C. ES SACLAY
DSM

SERVICE DE PHYSIQUE N

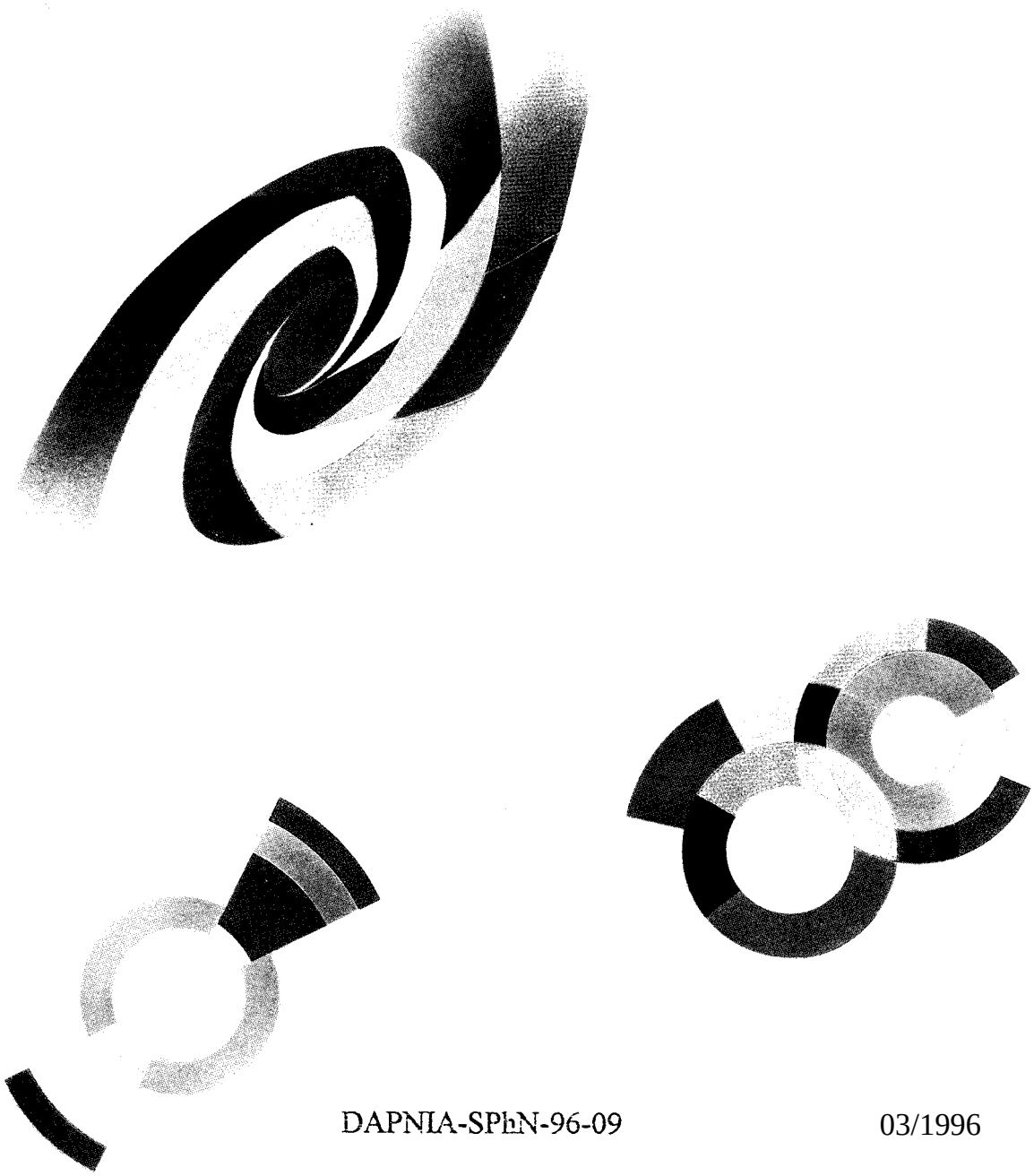

DAPNIA-SPhN-96-09 03/1996

Heating Nuclei with Light Ions at GeV incident energies

DAPNIA

E.C. Pollacco, J. Brzychczyk, C. Volant, R Legrain, L. Nalpas, D.S. Bracken, H. Breuer, R.G. Korteling, K. Kwiatkowski, K.B. Morley, E. Renshaw Foxford, V.E. Viola and N.R. Yoder.

Le DAPNIA (Département d'Astrophysique, de physique des Particles, de physique Nucléaire et de l'Instrumentation Associée) regroupe les activités du Service d'Astrophysique (SAp), du Département de Physique des Particles Elémentaires (DPhPE) et du Département de Physique Nucléaire (DPhN).

Adresse : DAPNIA, Bâtiment 141
CEA Saclay
F -91191 Gif-sur-Yvette Cedex

7èmes Journées d'Etudes SATURNE,
RAMATUELLE, 29 janvier -2 février 1996

Heating Nuclei with Light Ions at **GeV** incident energies.

E. C. Pollacco[1], J. Brzychczyk[1,3], C. Volant[1], R. Legrain[1], L. Nalpas[1], D.S. Bracken[2], H. Breuer[5], R.G. Korteling[4], K. Kwiatkowski[2], K.B. Morley[2], E. Renshaw Foxford[2], V.E. Viola[2] and N. R. Yoder[2]

[1]CEA D.+ PNIA/SPhN, CESaclay, 91191 Gif-sur-Yvette CEDEX, France.
[2]Dept. of Chem. & IUCF, Indiana Univ., Bloomington, IN47405, USA.
[3]Inst. of phys., Jagiellonian Univ. 30-059 Krakow, Poland.
[4]Dept of Chem., Simon Fraser Univ., Burnaby, BC, Canada.
[5]Dept " of Phys., Univ. of Maryland, College park, MD 20742, USA.

INTRODUCTION

The subject of hot nuclei draws a number of engaging problems. Broadly speaking one can divide the interest into three; the heating dynamics [1-3]; properties of hot nuclear matter [4] and the decay processes 5 All this is within the confines of a relatively small number of nucleons interacting through an interplay of short and long range forces [5]. In this contribution we report on a study of hot nuclei, where through an appropriate choice of incident channel and event selection. dynamical effects are attenuated and multifragmentation is limited. Herein, we aim at giving three preparatory results; (i) the ^{3}He(1.8 GeV) + ^{nat}Ag can be described using an intranuclear cascade, INC, model; (ii) through a suitable selection of events we give a limit of the excitation energy that a nucleus can absorb without breaking into large pieces; (iii) we show that corresponding alpha decay is consistent with an, evaporative process.

Before indulging in the experimental set-up, it is practical to adopt a general outlook of the reaction processes involved in light ion induced reactions at GeV.A incident energies. Within a BUU[6] description. the projectile nucleons are subject to n-n collisions and are then, more often than not, ejected over a time scale compatible with $\sim$15 fro/c. This primary process leaves behind an abundant number of energetic. π, Δ and nucleons. Over a time period covering say. 15 to 100 fro/c the residual system evolves through a sequence of dynamic evolutions with processes (π reabsorption, etc), in part, leading to thermalisation. As pointed out by Wang et al.[3], the coupling to the mean field could have a determining effect on the final channel through the formation of spatial density variation. However, we consider that at 1.8 GeV the consequences of these effects are less marked than at 4.8 GeV[3]. Beyond 100 fro/c the mean field settles down to give a predominantly thermalised hot nucleus. Herein we consider an INC

description, where beyond ~ 30 fm/c the resultant complex is assumed to have normal sherical, uniform density distribuitions with the energy being shared between thermal and rotational degrees of freedom. On average at 1.8 GeV, the angular momentum is $20\hbar$ and the residual mass varies weakly with the calculated excitation energy[7]. As for the calculations presented, all impact parameters are considered with each event generated by the INC code[1] being fed into an evaporative routine, EUGENE[8]. Where necessary the events are filtered by the experimental acceptance (code FILTER). No effort was made to adjust the parameters of the INC and EUGENE.

Experimental Set-Up

The experiment was performed at the Laboratoire National Saturne using ^{3}He beam at 1.8, 3.6 and 4.8 GeV . In this contribution we present the lower incident energy data set. The target was natural Ag of thickness 1.08 mg/cm^2. Briefly, the experimental set-up consisted of essentially four parts. (i) 'To measure leading protons AR COLE was used 9 This consists of a forward plastic wall made up of 28 fast plastics and mounted so as to have a hole in the center for the beam. Light from each plastic was read out by two photomultipliers and gives the energy loss and impact position. This assembly covered an angular range of approximately 2.5 to 12" and was positioned to give a minimum flight path from the target of 4 meters. (ii) To detect heavy fragments, HF, a circular hodoscope, DELTA, which includes 30 high field Si detectors w-as used. The target-detector flight path was 60 cm and covered angles between 5 to 10°. (iii) Light charged particles (Z $\leq$ 2), LCP, and intermediate mass fragments (Z $\leq$ 20), IMF, were detected in an array called IS iS 10 which contains 162 triple detector telescopes in a tight geometry. Each telescope is composed of a gas-ionisation chamber, a fully depleted .500 μm ion-implanted silicium detector and a 28 mm CsI(Tℓ) crystal. The geometrical acceptance is typically 70% and thresholds are better than 1 MeV.A. The charge, Z, resolution ranged up to 20. Mass resolution is obtained for those particles which punch through the Si crystal. (i v) A n active collimator assembly was employed to vetoe the beam halo particles reaching ISiS.

Possibly the only distinct signal of the reaction primordial time that we captured with our set-up are the fast leading protons. In fig. 1 we give the overall proton multiplicity in ARCOLE with a minimum trigger of 2 particles in IS iS. The lower energy threshold in ARCOLE is approximately 50 MeV for protons. The dashed histogram gives the filtered proton multiplicity from the INC calculations and illustrates the fair description of the data.

Analysis

Fig. '2 gives the superimposition of 26 mass vs velocity plots from DELTA for fragments under the minimum trigger condition. The mass was computed from the time between DELTA - ISiS and energy measurements. Correction due to time delay [11] and energy defect [12] were included. The latter was achieved through a coincident set-up with slowed down fission fragments in a separate measurement. Software velocity thresholds were set at 0.25 cm/ns. We remark that in light ion induced reactions it is expected that the highest yield of H F should be for mass values close to that of the target[13]. The shift seen in the figure towards a mean mass of ~ 70 amu is largely due

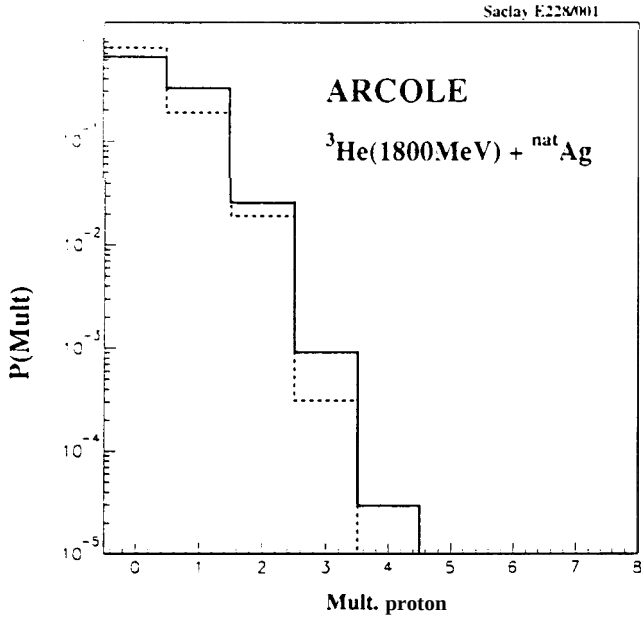

Figure 1. Probability for the multiplicity for high energy protons in the plastic wall ARCOLE with minimum trigger. The dashed histogram refers to the INC+EUGENE+ FILTER prediction.

to the target thickness energy threshold effects. It is important to note, however, that the fragments of interest here are the ones about (mass,velocity)=(45,0.6), which in fact are not strongly perturbed by the choice of target thickness.

Before detailing the analysis of how we assign excitation energies it is helpful to note and remark that; the data-model (INC+EUGENE+FILTER) comparison for events with minimum bias show a reasonable agreement for the global parameters. The total multiplicity, M_{tot}, is well described (fig. 3) for example, and this is also true for the total detected charge, IMF multiplicity, M_{IMF}, and so on. Less evident is the comparison of the linear momentum transfer. No inconsistency is found but the widths for the data and model are too wide to make a quantitive comparison. These results substantiate, in a circumstantial way, the model and allows us to examine our method to extract and correct the experimental excitation energies.

In this paragraph we describe the simple prescription we have employed to reconstruct what we call here, "thermal" excitation energy E_{th}, and mass, M_{th} . By thermal we refer to the energy and mass that is left over after the pre- equilibrium/cascade particles have escaped from the nuclear complex. Similarly, we consider Z_{th}. To compute these quantities experimentally we encounter three difficulties; (i) our set-up does not include a direct measure of neutron multiplicity and summed neutron kinetic energy. It is important to emphasise, that even with the present favourable choice of target, the calculated energy released through the neutrons can be as much as one half of E_{th}; (ii) detector geometrical acceptance and in particular the mass resolution at low energy; (iii) establishing a criteria of rejecting particles within an event which are considered of non-thermal descent. These points are of no revelation. Different groups have developed different techniques to reduce source of error. Item (i) and (ii), for example, have

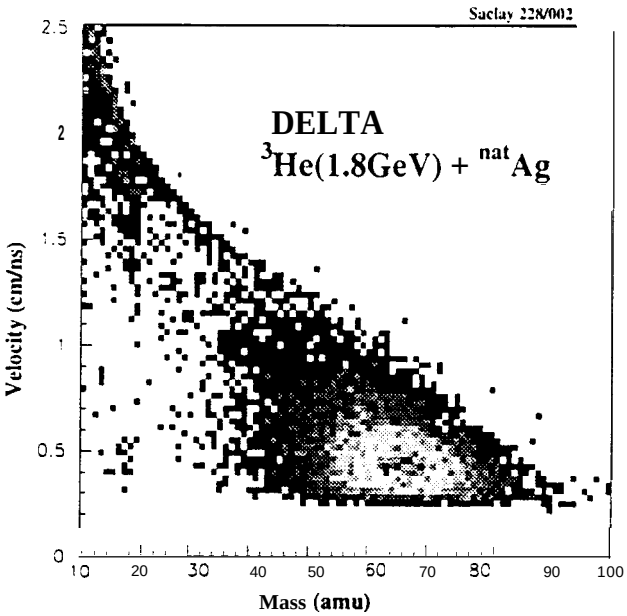

Figure 2. Residual mass versus velocity plot

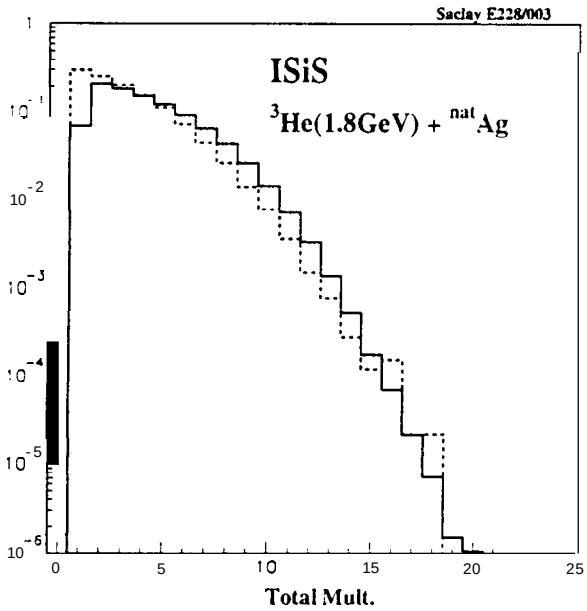

Figure 3. Probability for the total multiplicity data (solid histogram). The model predictions (dashed histogram) are normalised by a factor 1.2.

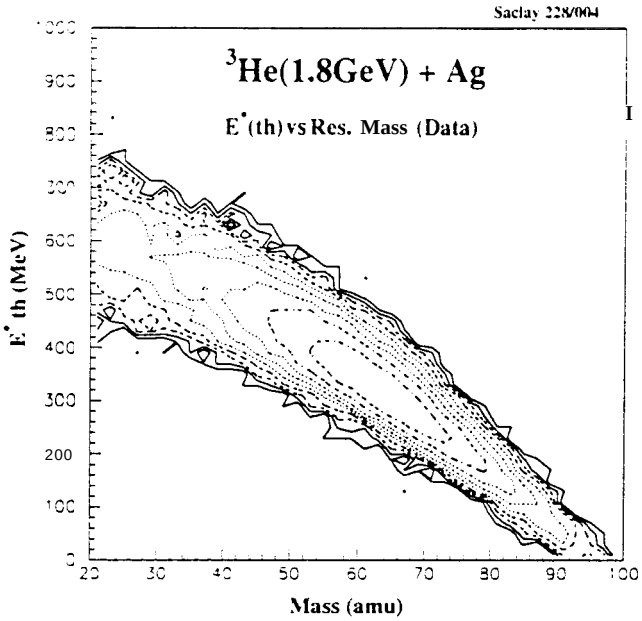

Figure 4. Experimental E_{th} as a function of residual mass.

been reasonably covered by the MBI + Ganil group at Cern [14]. The method employed here, and elsewhere [15,16], to account for (iii) is somewhat brutal; within an event, only those LCPs with KEs smaller than a given value are treated. As for the IMFs they have practically no pre-equilibrium component. The total detected M_{tot} mass, which includes the HF is then obtained event-by-event. Where only the charge is detected, the mass is derived through a function giving values in the valley of stability. In the case of low energy Z=1 these are given unit mass values. The total detected charge in ISiS and DELTA, Z_{th}, is obtained by transforming the HF mass into charge. The value of M_{th} is then obtained through a lookup table of ratios M_{th}/Z_{th} given by INC. The difference between M_{th} and M_{tot} gives the number of neutrons. Finally, E_{th} is obtained by summing over the KE of the selected particles and adding in the appropriate Q-values. For the neutrons we adopted a mean KE of 7.5 MeV/neutron, a value extracted from the INC+EUGENE code. It is important to stress that at this point we do not correct for geometrical acceptance. However with the above prescriptions and using the INC+EUGENE+FILTER as guide, we deduce the mean correction in extracted E_{th}. In the zone of interest, the correction in experimental E_{th} is of the order of 25%.

In fig. 4 we plot the residual mass as a function of E_{th}. This was obtained by demanding software triggers of a HF in DELTA for $M_{IMF} = 0$. Note that this condition on M_{IMF}, is equivalent to having ~40% probability to have, in the event, an undetected IMF. Further, the HF velocity and accompaning charge distribution for events which do have IMFs in coincidence indicates that fission is not a competing process for the higher E_{th}. Projecting a E_{th} spectrum with a window on the residual mass of (40,45) yields a Gaussian like peak. Correction for the acceptance gives a mean excitation energy of 625 MeV. As is evident from the figure, shifting the mass window to lower values increases this E_{th}.

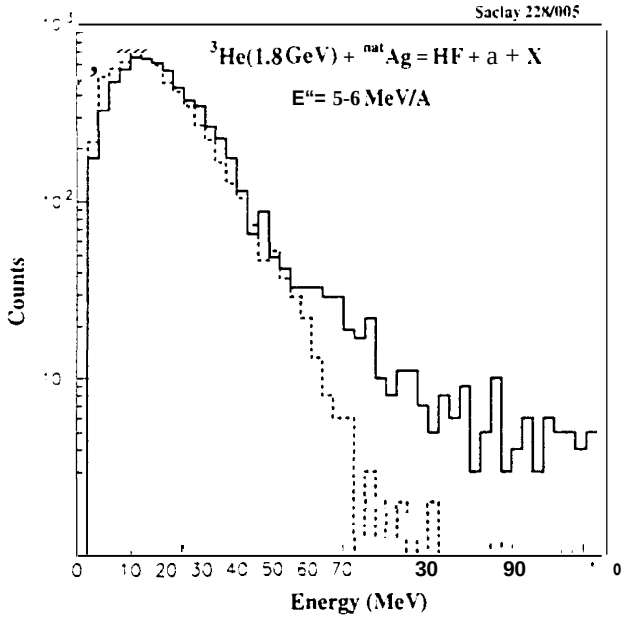

Figure 5. Energy spectrum for alphas in coincidence with HF for ϵ^* =5-6MeV/A.

The HF-coincident α (note no mass resolution in ISiS for Z=2 at low energy) particle spectra as a function of ϵ^*= E_{th}/M_{th} and M_{th} $\geq$35 have been extracted and compared with the INC+EUGENE+FILTER calculations. In fig. 5 the spectra with a window of ϵ^* = 5-6 MeV/A are compared. Other comparisons, such as mass of the HF, HF-M_{IMF} or HF-M_{tot}, are of equivalent merit.

Conclusion

In conclusion, we report on an experimental study of ^{3}He(1.8GeV)+^{nat}Ag where we detect LCP + IMF with a large geometrical coverage in conjuction with heavy fragments and fast protons in the forward direction. The global parameters with this configuration are effectively reproduced with an INC + EUGENE description. An attempt is made to extract the highest excitation energy reached that decays in a non-multifragmentary fashion. Values of ϵ^*/binding energy of 78% are obtained. The data-model comparison for the a-spectra indicate that at relatively high excitation energy the system can still decay through an evaporative process.

REFERENCES

1. J. Cugnon, Nucl. Phys. A462, 751 (1987).
2. K. Kwiatkowski, W.. A. Friedman, L. W'. Woo, V.E. Viola, E.C. Pollacco, C. Volant, S.J. Yennello Phys. Rev. C49, 1516 (1994).
3. G. Wang, K. Kwiatkowski, VE. Viola, W. Bauer, P. Danielewicz, pre-print, Indiana Report, INC-40007-106d, 1995.
4. S. Levit, P. Bonche, Nucl. Phys. A437, 426 (1985).

5. D. H. E. Gross, Rep. Ping. P hys. 53, 605 (1!)!}()).
6. W. Bauer. C.K. Gelbke. S. Prat 1. Ann. Rev. Nucl. Part Sci. 42. 77 (1992).
P. Danielewicz Phys. Rev. C 51. 716 (1995).
7. .1. Brzychczyk, E.C. Pollacco. C. Volant. R. Legrain, K. Kwiatkowski. D. Braken. K.B. Morley. E. Renshaw Foxford. V. E. Viola. N. R. Yoder. W. .4. Friedman. R.G. Korteling. H, Breuer. J. Cugnon. XXXIII Winter Meeting on Fuel. Phys. Bormio. Italy.
8. Modified version of EUGENE. D. Durand. Nucl. Phys. A541. 266 (1992).
9. Y. Terrien et al.. Phys Lett. B294. 40 (1992).
10. K. Kwiatkowski et al.. Nucl. Instr. Meth. A360. 5 (1995),
11. S.B. Kaufman, et al.. Nucl. Instr. Meth. 115. 47(1974).
12. H.O. Neidel. H. Henschel. Nucl. Instr. Meth. 178. 137 (1995).
13. S.B. Kaufman and E. P. Steinberg, Phys. Rev. C22. 167 (1980)
14. J. Galin, Int. Nucl. Conf.. Beijing, China. 1995.
15. A. Hirsch, (Purdue) contribution to this workshop,
16. K. Kwiatkowski et al., Phys. Rev. Lett. 74. 3756 (1995).
K. B. Morley et al., Phys. Lett. B355. 52 (199.5).